Ionic thermoelectric supercapacitors

Dan Zhao, Hui Wang, Zia Ullah Khan, J. C. Chen, Roger Gabrielsson, Magnus Jonsson, Magnus Berggren and Xavier Crispin

Zhao, D., Wang, H., Ullah Khan, Z., Chen, J. C., Gabrielsson, R., Jonsson, M., Berggren, M., Crispin, X., (2016), Ionic thermoelectric supercapacitors, *Energy & Environmental Science*, 9(4), 1450-1457.
https://doi.org/10.1039/c6ee00121a

Ionic Thermoelectric Supercapacitors

Dan Zhao[(a)], Hui Wang[(a)], Zia Ulla Khan[(a)], Jincan Chen[(b)], Roger Gabrielsson[(a)], Magnus P. Jonsson[(a)], Magnus Berggren[(a)] and Xavier Crispin[(a)]*

[(a)]*Department of Science and Technology,Campus Norrköping, Linköping University,S-60174 Norrköping, Sweden,*

[(b)]*Department of Physics, Xiamen University, People's Republic of China*

** Corresponding author: Xavier.crispin@liu.se*

Temperature gradients are generated by the sun and a vast array of technologies and can induce molecular concentration gradients in solutions via thermodiffusion (Soret effect). For ions, this leads to a thermovoltage that is determined by the thermal gradient ΔT across the electrolyte, together with the ionic Seebeck coefficient α_i. So far, redox-free electrolytes have not been explored in thermoelectric applications due to a lack of strategy to harvest the energy from the Soret effect. Here, we demonstrate the conversion of heat into stored charge via the ionic Soret effect in an Ionic Thermoelectric Supercapacitor (ITESC), thus providing a new means to harvest energy from intermittent heat sources. We show that the stored electrical energy of the ITESC is proportional to $(\Delta T\alpha_i)^2$ and that its α_i reaches beyond 10 mV/K. The resulting ITESC can convert and store several thousand times more energy as compared to a traditional thermoelectric generator connected in series with a supercapacitor.

INTRODUCTION

Various thermoelectric concepts are currently under investigation for conversion of thermal energy into electrical energy, with the goal to provide efficient thermoelectric systems. First, electronic charge carriers in a conductor thermodiffuse when subjected to a temperature gradient, which leads to a thermovoltage known as the Seebeck voltage. Thermoelectric generators (TEGs) that utilize the Seebeck effect are typically composed of semi-metals [1, 2], inorganic semiconductors [3, 4], and electronically conducting polymers have also recently been explored [5]. Secondly, thermovoltages can originate from the thermogalvanic effect, which results from temperature-dependent entropy changes during electron transfer between a redox molecule and an electrode [6]. Hence, thermogalvanic cells are based on electrolytes with redox couples, such as ferricyanide/ferrocyanide. The Soret effect [7] of redox free electrolyte, i.e. from ionic charge carriers constitute yet a third thermoelectric concept that, to the best of our knowledge, has not previously been considered for energy harvesting. Analogous to the electronic Seebeck effect, the Soret effect is a result of thermo-diffusion of ions in an ionic solid [8, 9] or electrolyte [10]. This produces an ionic concentration gradient and a corresponding thermo-voltage that is governed by the temperature difference across the material and the ionic Seebeck coefficient α_i.

For a traditional thermoelectric leg, composed of a semiconductor and two metal contacts, a constant electrical power can be provided to an external load by imposing a temperature gradient along the metal-semiconductor-metal stack. The same harvesting principle is, however, not directly applicable if the semiconductor is replaced by an electrolyte solution with ions as charge carriers. The reason for this is that the thermo-diffused ions are blocked at the surface of the metal electrode and cannot pass through the external circuit. Instead, the ions will be accumulated in excess at the metal surface where they form an electric double layer capacitor (EDLC) [11]. Our novel approach utilizes this EDLC principle and harvest energy from the ionic thermoelectric effect by charging and discharging carbon nanotube super-capacitor electrodes. The resulting device is here referred to as an ionic thermoelectric supercapacitor (ITESC). In addition to demonstrating and characterizing this novel concept, we compare the characteristics of the ITESC with those obtained for a traditional electronic thermoelectric generator (TEG) coupled to a supercapacitor (SC).

RESULTS

1. Thermoelectric characterization of PEO-NaOH.

We choose a low molecular weight PEO ended with alcohol groups (Mw=400g/mol) as the electrolyte, because it is non-volatile and can withstand relatively high temperatures (<120°C). The facilitated thermoelectric effect is stable since there is no solvent evaporation and degradation for large ΔT over long period of times. We added NaOH to the liquid PEO ($C_{(NaOH)}$=0.75mM) to transform the terminating alcohol groups (-C-OH) into anionic alkoxide end-groups (-C-O^-Na^+). [12] Nuclear magnetic resonance (1H-NMR) and Fourier Transform Infrared Spectroscopy (FTIR) confirm that the reaction has occurred (fig. S1 and S2 in supplementary information 1). The resulting electrolyte is composed of polymeric anions that are very weakly mobile and mobile Na^+ cations. The ionic conductivity measured by impedance spectroscopy is 8.13×10^{-5}S/cm at room temperature and the activation energy for the ionic transport is 476meV (see supplementary information 2). We investigate the thermoelectric properties of the PEO-NaOH solution. The thermoelectric liquid is injected into a small cylindrical chamber (1mm thick, diameter of 10mm). Planar Au electrodes are evaporated on both sides of the chamber and are in direct contact with the polymer electrolyte (fig.1a). In order to monitor the temperature difference between the two electrodes, we fabricated thermistors under the electrodes (details are provided in supplementary information 3). At any given ΔT, the corresponding Soret-induced open voltage can be obtained. This is exemplified in Fig. 1b during heating one side of the device while cooling of the other side. The thermovoltage induced by different ΔT was investigated in the temperature range between 25°C and 35°C. For each ΔT, the voltage was measured 5min after stabilization. The results are presented in Fig. 1c and demonstrate that V_{thermo} varies linearly with ΔT. The slope of the linear fit gives an ionic Seebeck coefficient of +11.1 mV/K for the PEO-NaOH electrolyte. The thermovoltage originates from non-compensated thermodiffusion of cations and anions, with an overall sodium cation accumulation at the cold electrode, as expected since alkoxylate and carboxylate anions are mostly immobile. The magnitude of the ionic Seebeck coefficient is remarkably high. Indeed for Na^+ in a diluted aqueous solution, the heat of transport Q* is about 3 kJ/mol, [13] giving an expected Seebeck coefficient of $\alpha_{Na+}=Q^*/N_a|e|T=0.1$mV/K, where N_a is the Avogadro number and |e| is the

charge of an electron. This is 100 times smaller than what is found for the PEO-NaOH electrolyte. The Born model [14] allows a first estimate of the heat of transport [15] and the thermopower. [16] In this model, the square of the dielectric constant of the medium is inversely proportional to the Seebeck coefficient. Although the static dielectric constant of PEO (ε_0=36.1 at 20°C) is lower than that of water (ε_0=80.6 at 20°C), its temperature variation (dε/dT=0.02) is negligible compared to water (dε/dT=0.49). As a result of those compensating effects, we conclude that the large difference in the thermovoltage of Na^+ in water and in PEO cannot be attributed to the difference in dielectric constant (see supplementary information 4). Thermodiffusion is a complex process that also involves the interaction and entropy change between the solvent and the ions.[17] The complexity is not reduced with the presence of polymer chains. For instance, ions in polyelectrolyte and salt solution are expected to have a Soret coefficient 100 times larger than a salt solution without polyelectrolyte. [18] This could be one origin for the large ionic Seebeck coefficient measured for PEO-NaOH. Other reports also indicate large thermoelectric coefficients for polymer electrolyte membranes, from few mV/K to around 500 mV/K [19]. Aside from the major ionic Seebeck voltage, there may be another minor contribution due to a thermogalvanic voltage associated with the Faradic process involved in the leakage current [20]. Regardless of reason, it is clear that ionic polymer solutions can provide remarkably high Seebeck coefficients, and relatively low thermal conductivity of 0.216 $wm^{-1}k^{-1}$, as measured by the 3-omega method (see supplementary information 5), which may be found useful in various applications.

The Au electrodes of the device can be functionalized with self-assembled multi-wall carbon nanotubes to form a supercapacitor (fig. 1a) (CNT, detailed preparation protocols are provided in the supplementary information 6). CNTs self-assembled onto the Au-contact provide intercalation of electrolyte components, thus providing a relatively much higher capacitance value over a projected area unit. Both Au and CNT electrodes are electrochemically stable over a potential window much wider than what is measured from the induced thermovoltage, which means that no Faradic processes related to electrode deterioration are involved in the ITESC measurements. Similar saturation of V_{thermo} vs. time (inset fig. 1b) and evolution of V_{thermo} vs. ΔT (fig.1c) are obtained using both Au and CNT electrodes, which indicates that the nature of the electrodes does not play a role and that the thermovoltage is an intrinsic property of the polymer electrolyte.

2. Capacitance properties characterization

Carbon nanotube films have previously shown to be suitable as electrodes in supercapacitors,[21] primarily due to their large surface area [22]. Application of a voltage over the PEO-NaOH capacitor induces migration of the cations towards the negatively charged CNT electrode, at which an electric double layer (EDL) is formed (illustrated in fig 2a). We compare the electrical characteristics of three devices that are based on the same polymer electrolyte PEO-NaOH, but with different electrodes: two different amounts of CNT assembled onto Au electrodes (we define them as thick and thin CNT electrodes) and the bare gold electrode. Before exploring the effect of a thermal gradient, we characterize the capacitors electrically (at 22°C) by impedance spectroscopy and cyclic-voltammetry.

With impedance spectroscopy, an alternating voltage $V_{ac}(f)$= 5 mV is applied across the electrolyte-based supercapacitors, the polarization characteristics of the electrolyte strongly depend on the frequency *(f)* [23, 24] and the total complex impedance $Z_{Tot}(f)$ is measured. Fig. 2b shows Nyquist plots, i.e. the real $Z_{Re}(f)$ vs. the imaginary $Z_{Im}(f)$ part of the impedance of the device with Au, thin and thick CNT electrodes, in the frequency ranging from 0.001Hz to 100kHz (without any DC bias). As shown, all the Nyquist plots consist of two distinct parts including a distorted semicircle at the high frequency region and a sloped line in the low frequency region. The x-intercept in the Nyquist plots represents the equivalent series resistance (R_s), which corresponds to the electrolyte solution resistance. R_s is almost identical for the different devices and is about 1.5kΩ. Also, the presence of a semicircle indicates that an additional resistive element (R_p) acts in parallel and it is associated to a low-frequency leakage resistance (see equivalent circuit in the inset of fig. 2). The equivalent circuit parameters (table 1) have been obtained by fitting the experimental Nyquist spectra. For the Au electrodes, the capacitance is around 5μFcm^{-2}, which is typical of EDLCs [25]. Because of the extremely high effective surface area of the CNT electrode networks (≈120-430m^{2}g^{-1}) [26], the specific capacitance is typically larger than for a planar metal electrode [19] and reaches in our case 1.03mFcm^{-2} for the thick CNT electrodes and 0.48mF cm^{-2} for the thin electrodes.

Typical cyclic voltammetry (CV) characteristics of the different devices are presented in Fig 2c for the same scan rate (dV/dt=10mV/s). The devices exhibited a near-ideal rectangular shape, indicating purely capacitive behavior. The amplitude of the current is proportional to the capacitance of the electrodes ($I=-CdV/dt$): small for Au and large for CNT electrodes. The capacitance of the thick CNT electrode is estimated to about 0.95mFcm^{-2}; while for the thin CNT electrodes it is about 0.48mFcm^{-2}. This is consistent with the result from the impedance measurements.

The charge and discharge characteristics of the SCs are studied by electric potential static charge-discharge measurements (Fig. 2d). For the charging procedure, a power supply, R_{load} and SCs are connected in series, and the voltage across R_{load} is recorded. Around 5 min after the recorded voltage stabilizes, the power supply is replaced by a short at those two electrodes, and the discharging current is obtained by recording the voltage drop over R_{load}. The device is charged with a constant potential of 50mV. Two measurements with different charging times are shown in the graph, indicating that the discharging curve does not change for prolonged charging times. This means that the stable leakage current, which is most likely a Faradic current between the electrode and the electrolyte, does not contribute to the accumulated charge on the CNT electrodes. In other words, the amount of charge transferred to and stored in the capacitor will always be less than the calculated charge using $Q=CV_{load}$, since a part of the charging voltage is lost across R_{load} even at full charging. We infer that this leakage current is related to the parallel resistance (R_p) in the equivalent circuit. After charging, the stored charge may gradually vanish due to self-discharging. We investigate this by measuring the decay of the open voltage (without connecting R_{load}) in Fig. S7 (see supplementary information 7). The device with thick CNT electrodes provides significantly better charge retention than the device with thin CNT electrodes. For this reason, we choose to focus the rest of the investigation on the PEO-NaOH based supercapacitor with thick CNT electrodes.

3. Demonstration of the ionic thermoelectric supercapacitor

We now demonstrate the first ITESC, by combining the promising thermoelectric properties of the PEO-NaOH solution and the high capacitive performance of the device when sandwiched by CNT-Au electrodes. The ionic thermoelectric effect will act as an internal electric generator that can charge the EDLC of the supercapacitor. In brief, the ITESC concept is based on the following expected mechanisms. (i) First, a ΔT is applied over the electrode-electrolyte-electrode stack to induce a thermovoltage $V_{thermo}=\alpha_i \Delta T$. (ii) By connecting an external load resistance (R_{load}), the ionic thermovoltage is used to charge the supercapacitor. (iii) After charging, R_{load} is disconnected (open circuit) and the heater is switched off. In this step, the thermovoltage should decay to zero, such that the open circuit potential is governed only by the voltage drop (of opposite sign) induced by stored charge. (iv) Finally, the device can be discharged by connecting the ITESC stack to an external circuit including R_{load}.

We demonstrate the ITESC concept in Fig 3a. (i) First, a ΔT of 16 K is established across our device while V_{thermo} is recorded. As expected, V_{thermo} increases during heating until it reaches a stable thermovoltage of around 180mV. (ii) Next, R_{load} (100kΩ) is connected and the voltage across it (V_{load}) is recorded. V_{load} decreases rapidly and reaches a stable value around 50mV. This is the charging curve of the device. The decrease of V_{load} during charging is attributed to charge being transferred to the capacitor, which induces a potential of opposite sign that compensates the thermovoltage. The residual voltage is related to the electronic leakage current, which results in a non-zero voltage drop over R_{load} also after full charging. Hence, the effective charging voltage ($V_{effective}$) is reduced from 180 mV by 50 mV to around 130 mV. The predicted $V_{effective}$ can also be estimated from V_{thermo} (1-$R_{\mathrm{load}}/(R_{\mathrm{load}}+R_{\mathrm{p}}+R_{\mathrm{s}})$), which with the values in table 1 for the thick CNT electrodes gives $V_{effective}$=150mV, which is close to the measured value.

We compare the charging behavior of the ITESC exposed to a varied temperature gradient versus charging achieved by applying an external voltage source (blue curve in fig 2b). The two charging curves, obtained by varying the voltage versus changing the ΔT, overlays perfectly with each other. The good agreement between the two curves indicates that the two charging methods have almost the same charging behavior. This means that the thermoelectric effect for ΔT (T_{average}) is equivalent to an internal electric generator ($V=\alpha_i \Delta T$). Additional results comparing electrical and thermoelectric charging are provided in the Supporting Information 8 (fig. S8a). (iii) After completed charging, the heating is turned off and the circuit is kept open. As the thermovoltage decays, the recorded V_{thermo} decreases to negative values, which infers that charges have indeed been transferred to the CNT electrodes by ITESC. (iv) The final part of the curve in Fig 3b demonstrates that the supercapacitor is able to discharge and provide useful energy to a load, as evaluated in more detail below. As expected, repeating the ITESC experiment for a device with Au electrodes instead of CNT electrodes do not provide any measurable charging or discharging (fig. S8b). Repeating the ITESC process over multiple cycles produces highly reproducible charge-discharge current evolutions (Fig S9). This demonstrates not only the stability of the device but also its true potential for harvesting electricity from intermittent heat sources.

4. Evaluation of charge transfer during charging and discharging

During the charging step, the thermoelectric charging of the ITESC shows very similar output current through R_{load} as for electric charging of the supercapacitor at a voltage equals to the thermovoltage, and both charging principles also lead to the same level of leakage current. We therefore propose that the ITESC can effectively be described by an equivalent circuit that is similar to electrical charging (Fig. 3b), where the voltage source is equivalent to the thermovoltage, and the rest is composed of a load resistance and a sub-circuit corresponding to the supercapacitor (as derived in section 2). During charging, the generator provides a thermovoltage $\alpha_i \Delta T$, while the capacitor will be shorted before discharging takes place. We stress that this equivalent circuit does not describe the complete ITESC circuit, for which the voltage drop over the capacitor in fact starts at $\alpha_i \Delta T$ and decreases during charging, but it is implemented to describe the effective voltage that goes into charging of the supercapacitor. The time constant for charging in this equivalent circuit is $\tau = C(R_s + R_{load})$, and we use 5τ as charging time when calculating the stored charge in the capacitor (more details can be found in supplementary information 10).

The amount of charge transferred to the capacitor is calculated by integrating the current flowing through the capacitor ($I_{\text{capacitor}}$) during charging or discharging. In turn, these current is obtained by measuring the voltage over the R_{load} and by subtracting the time-dependent leakage current (I_{leakage}), which does not contribute to the charging process. We estimate the leakage current from the voltage drop over the capacitor ($V_{capacitor} = \Delta T \alpha_i - V_{load} - V_s$) divided by R_p and V_s is the voltage drop over the internal series resistance. In first approximation, R_s is negligible compared to R_{load}, such that the transferred charge is:

$$Q_{\text{charging}} = \int_{\text{charging}} (I_{\text{load}} - I_{\text{leak}})\,\mathrm{dt} = \int_{\text{charging}} \left(\frac{V_{\text{load}}}{R_{\text{load}}} - \frac{\alpha_i \Delta \mathrm{T} - V_{\text{load}}}{R_{\text{p}}}\right)\mathrm{dt} \quad (1)$$

Figure 3c shows the calculated charge stored for different ΔT during charging. Because $Q_{\text{charging}} = CV_{\text{effective}}$ at full charging, and $V_{\text{effective}} = \Delta T \alpha_i (1 - R_{\text{load}}/(R_{\text{load}} + R_p + R_s))$, the charge is expected to be linearly proportional to the temperature gradient according to:

$$Q_{\text{charging}} = C\Delta T \alpha_{\text{i}} \left(1 - \frac{R_{\text{load}}}{R_{\text{load}} + R_{\text{p}} + R_{\text{s}}}\right) \quad (2)$$

Figure 3c shows that the amount of charge increases approximately linearly with ΔT with a slope of 8.3 $\times 10^{-6}$ C/K. This is of close to 8.8×10^{-6} C/K, as predicted by equation 2. Similarly, the charge transferred during discharging also increases with ΔT, although the trend is less clear and there is a larger spread in the values. Notably, there is an apparent loss for the charge transferred during discharging compared to charging. This can be attributed to self-discharge during the time t_{eq} of temperature equilibration (step iii in Fig. 3a, see supplementary information7). The loss in stored charge during t_{eq} can fully explain why $Q_{discharge}$ is lower than Q_{charge} in the ITESC measurements (Fig. 3a and 3b). Based on multiple measurements with similar equilibration times (t_{eq}=550s-650s), the ratio $\beta = Q_{discharge}/Q_{charge}$ upon TE charging at 50 mV (ΔT= 4.5°C) was measured to be around 27% (table 2). Almost the same value of β (approximately 28%) is measured when the same supercapacitor is instead electrically

charged (ΔT=0) at $T_{average}$ and when the discharge is triggered 600s after charging. If the discharging is triggered directly after electrical charging (within 1s), the self-discharge has a minor effect and β reaches values as high as 94%. We note that because the ITESC principle requires a waiting step between charging and discharging, future devices with lower self-discharge should provide better ratios.

5. **Stored charge and energy**

Fig. 4a shows $Q_{charging}$ (black squares) and the energy (red dots) transferred to the capacitor during charging (the current curves plotted versus time are provided in Fig. S10 in supplementary information 11). $Q_{charging}$ is relatively insensitive to R_{load} for values up to around 20kΩ, after which it decreases as R_{load} becomes comparable to R_p. Note that for R_{load} values close to R_s, the accurate expression of $V_{effective} = \Delta T\alpha_i(1-(R_{load}+R_s)/(R_{load}+R_p+R_s))$. The experimental results can be accurately expressed by $Q_{charging}=CV_{effective}$ (dashed black line), where C is the surface capacitance (1.03mF/cm^2). The measured energy stored per area in the capacitor is 1.35μJ cm^{-2} for ΔT=4.5K and R_{load} <20kΩ, but decreases for large R_{load} (red dot). This evolution is also in agreement with the theoretical prediction (dashed red line) ($E_c=1/2Q_{charging}^2/C$).

The energy per area is found to increase quadratically with the applied temperature gradient, approximately as $E= ½C(\Delta T\alpha_i)^2$. In an ITESC, the stored electrical energy can be expressed as a function of the Seebeck coefficient of the electrolyte. This expression can be further revised for a realistic device with a leakage current as $E=½C(\Delta T\alpha_i-V_s-V_{load})^2$. The latter overlaps the experimental data perfectly (Fig. 4b). Also, the experimental values for the ITESC are close to the experimental data (blue open triangle in fig. 4b) obtained for a circuit made of the SC (ΔT=0) and a power supply providing a voltage equal to the thermovoltage (so called electrical charging). The latter fits the theoretical expression $E= ½CV^2$. The extrapolated energy density for ΔT=10K is 33.8kJ/kg (9.4Wh/kg). Importantly, the energy density for large temperature gradients can be high, because the ionic thermovoltage of the polymer electrolyte system is exceptionally large. For the sake of comparison, Li-polymer batteries have an energy density of about 200Wh/kg. [24] Hence, in principle, the ionic thermoelectric effect of polymer electrolytes can be used to charge partially any type of supercapacitors or batteries.

In order to pinpoint the unique feature of the ITESC, we now compare its electrical characteristics with that predicted for a single leg thermoelectric generator (TEG) based on Bi_2Te_3 connected in series to the supercapacitor (SC). Since the Seebeck coefficient of Bi_2Te_3 (190μV/K) [1] is more than 50 times lower than PEO-NaOH (11.1mV/K), the resulting energy stored would be 2500 times lower (Fig. 4c). Hence, the ITESC is a very attractive solution compared to existing state-of-the-art technology when it comes to harvesting and storing electricity from an intermittent heat source.

We evaluate the efficiency η of the ITESC in converting heat to electricity; which is defined as $\eta=E_{out}/Q_{in}$, i.e. the ratio between the electrical energy that is generated and stored in the ITESC from the charging (E_{out}) and the total heat absorbed over one full ITESC cycle (Q_{in}). The dominant term is the thermal energy passing through the device during the time needed for the ions to slowly thermodiffuse and establish a stable V_{open} (t_{st}) (interval (i) in Fig. 3a). The efficiency for a full cycle

reaches 6× 10^{-6} % at low R_{load} and ΔT=4.5 K. Note that, if we consider only the heat to electricity conversion during the charging interval (integrating over the interval (ii) in Fig. 3a, i.e not over the full cycle), the "peak" efficiency of the measured devices reaches about 5× 10^{-4} % for ΔT=4.5 K. In the supporting information, we show that the total efficiency η can reach about 0.1% through the optimization of the device's architecture and the use of a large temperature gradient ΔT=100 K. We stress that the efficiency is 2500 times higher than that of a circuit composed of a SC connected in series with a conventional TEG.

We have demonstrated for the first time that the Soret effect in a polymer electrolyte leads to significant ionic thermoelectric effect that could be used to charge a supercapacitor. The presented ITESC device requires a fluctuation in the applied temperature gradient to function, which makes the concept suitable for intermittent heat sources, such as the sun. We discuss potential improvements of the ITESC concept, and predict the heat-to-electricity charging conversion efficiency to be able to improve if good thermoelectric electrolytes are designed with low specific heat capacitance, low thermal conductivity, large Seebeck coefficient and high ionic conductivity. Importantly, all materials constituting the ITESC (polymer and inorganic salts) are fully compatible with industry processing. Beside this first proof of concept, much more research and technology development are required to truly investigate the potential of the ITESC.

Methods

Materials. Polyethylene oxide (PEO, Mw: 400g/mol) is purchased from Fluka and used as received. Sodium hydroxide (NaOH), sodium hydride (NaH) and multi-walled carbon nanotube (m-CNTs, diameter: 5-9nm, length: 5μm) are purchased from Sigma-Aldrich.

Characterization. The effective capacitance and phase angle of PEO-NaOH is measured by impedance spectrometer (an Alpha high-resolution dielectric analyzer, Novocontrol Technologies GmbH, Hundsangen, Germany). The ac voltage 5 mV is applied while sweeping the frequency from 1×10^5Hz to 1×10^{-2}Hz. The effective capacitance per area is calculated the capacitive reactance (X_c=-Z_{Im}) via $C_{eff}(f)=[2\pi f X_c(f)A]^{-1}$, where A is the surface area of the electrodes with disregard to their porosity, while the frequency-dependent phase angle $(\varphi(f))$ was obtained from the real and the imaginary parts of the impedance via $\varphi(f)=tan^{-1}(Z_{Im}/Z_{Re})$.

The cyclic voltammetry was carried out using a μAutolab potentiostat (Eco Chemie, Utrecht, Netherlands) in the potential range of 0-0.2V at a scan rate of 10mVs^{-1}.

Thermo power measurements are carried out by sandwiching the samples by a pair of partier element. Voltage difference (ΔV) between two electrodes is recorded by a nanovoltmeter (Keithley Instruments, Inc., model 1282A). ΔV is averaged by reversing the polarity of each Seebeck measurement to eliminate the unipolar and off-set voltages. Temperature difference (ΔT) between two electrodes is measured using two thermistor beneath the Au electrodes used to measure the thermo-voltage. The two thermistors are made of narrow and thin Au lines vacuum deposited on the glass substrate. The thermistor are deposited with a 1 μm thick Si_3N_4 before the evaporation of the top Au electrode, and

calibrated in a climate chamber. The Seebeck coefficient is defined as $\alpha = \Delta V/\Delta T - \alpha_{Au}$. The Seebeck coefficient and conductivity are measured at 21°C.

The thermal conductivity of PEO-NaOH solution is measured using the differential 3ω-method, explained in more details in the supplementary information. A sinusoidal input current of tunable frequency ω, generated from an arbitrary waveform generator (AFG3000 from Tektronix), is applied to an insulated narrow metal heater with the liquid in the cavity on top. The third harmonic component 3ω of the voltage at the terminals of heater is measured with a lock-in amplifier (Stanford Research SR850). The reference measurement is performed inside cryogenic probe station from Janis under vacuum and the measurements with cavity filled with a liquid are performed in ambient environment at a temperature of 22°C.

Device Fabrication. A glass substrate is patterned with two Au thermistors (10μm width) by thermal evaporation and photolithography. Then 1μm thick Si_3N_4 is deposited by CVD as an insulation layer. And two round Au electrodes are patterned by thermal evaporation (10mm diameter).

Both the prepared glass substrate and PDMS (1mm thickness) are exposed in UV plasma for 3 mins, then contacted and baked at 70°C in oven for 10mins, then a cavity of 0.0785cm^3 is obtained.

PEO-NaOH solution with concentration of 3wt % is prepared and stirred before use. The solution is then injected into the chamber.

For devices with CNT electrodes, two electrodes (Au thermal evaporated) are UV plasma treated for 3min, and then drop-casting certain amount of CNT aqueous solution (0.1%). After the solution is dry, rinse the electrode with acetone and water, dry them by nitrogen gun.

Acknowledgements

The authors acknowledge the European Research Council (ERC-starting-grant 307596), the Swedish foundation for strategic research (SSF), the Knut and Alice Wallenberg foundation (KAW), The Swedish Energy Agency and the Advanced Functional Materials Center at Linköping University.

References

1. Poudel, B., et al., *High-thermoelectric performance of nanostructured bismuth antimony telluride bulk alloys.* Science, 2008. **320**(5876): p. 5.
2. Snyder, G.J. and E.S. Toberer, *Complex thermoelectric materials.* Nature Materials, 2008. **7**(2): p. 10.
3. Laiho, A., et al., *Controlling the dimensionality of charge transport in organic thin-film transistors.* Proceedings of the National Academy of Sciences, 2011. **108**(37): p. 15069-15073.
4. Hochbaum, A.I., et al., *Enhanced thermoelectric performance of rough silicon nanowires.* Nature, 2008. **451**(7175): p. 163-165.
5. Sun, Y.M., et al., *Organic Thermoelectric Materials and Devices Based on p- and n-Type Poly(metal 1,1,2,2-ethenetetrathiolate)s.* Advanced Materials, 2012. **24**(7): p. 6.
6. Hu, R., et al., *Harvesting Waste Thermal Energy Using a Carbon-Nanotube-Based Thermo-Electrochemical Cell.* Nano Letters, 2010. **10**(3): p. 838-846.
7. Eastman, E.D., *Theory of the soret effect.* Journal of the American Chemical Society, 1928. **50**(2): p. 283-291.

8. Howard, R.E.L., A. B., *Thermoelectric Power of ionic crystals.* Discussions of the Faraday's society, 1957. **23**: p. 113-121.
9. Girvin, S.M., *Thermoelectric Power of Superionic Conductors.* Journal of Solid State Chemistry, 1978. **25**(1): p. 65-76.
10. Tyrrell, H.J.V., Taylor, D. A., Williams, C. M., *The 'Seebeck Effect' in a purely ionic system.* Nature 1956. **177**: p. 2.
11. Kisza, A., *The capacitance of the electric double layer of electrodes in molten salts.* Journal of Electroanalytical Chemistry, 2002. **534**(2): p. 99-106.
12. Xiao, Y., J. Jiang, and H. Huang, *Chemical dechlorination of hexachlorobenzene with polyethylene glycol and hydroxide: Dominant effect of temperature and ionic potential.* Scientific reports, 2014. **4**. DOI:10.1038/srep06305
13. Snowdon, P. and J. Turner, *The concentration dependence of the Soret effect.* Trans. Faraday Soc., 1960. **56**: p. 1812-1819.
14. Born, M., *Volumes and heats of hydration of ions.* Z. Phys, 1920. **1**: p. 45-48.
15. Agar, J., C. Mou, and J.L. Lin, *Single-ion heat of transport in electrolyte solutions: a hydrodynamic theory.* The Journal of Physical Chemistry, 1989. **93**(5): p. 2079-2082.
16. Petit, C.J., K.E. Renner, and J.L. Lin, *The Entropy of Transport of NaCl and KCl at 30 ^{o}C.* Journal of Physical Chemistry, 1984. **88**(12): p. 2.
17. Marcus, Y., *Effect of Ions on the Structure of Water: Structure Making and Breaking.* Chemical Reviews, 2009. **109**(3): p. 25.
18. Leaist, D. J., L. Hao, Very large separations of polyelectrolyte in salt solution. J. CHEM. SOC. FARADAY. TRANS., 1994. 90(13): p. 1909.
19 Tasaka, M., Thermal membrane potential and thermoosmosis across charged membranes. Pure Appl. Chem., 1986. **58**(12): p. 1637.
20 Bonetti, M., S. Nakamae, M. Roger, and P. Guenoun, Huge Seebeck coefficients in nonaqueous electrolytes. J. Chem. Phys. 2011. **134**: p. 114513.
21. Niu, C., et al., *High power electrochemical capacitors based on carbon nanotube electrodes.* Applied Physics Letters, 1997. **70**(11): p. 1480-1482.
22. Zhang, L.L. and X. Zhao, *Carbon-based materials as supercapacitor electrodes.* Chemical Society Reviews, 2009. **38**(9): p. 2520-2531.
23. Colomban, P., *Proton Conductors: Solids, membranes and gels-materials and devices*. Vol. 2. 1992: Cambridge University Press.
24. Larsson, O., et al., *Insulator Polarization Mechanisms in Polyelectrolyte-Gated Organic Field-Effect Transistors.* Advanced Functional Materials, 2009. **19**(20): p. 3334-3341.
25. Bard, A. and L. Faulkner, *Electrochem. Methods.* Fundam. Appl.. Wiley, New York, 2001.
26. Frackowiak, E. and F. Béguin, *Carbon materials for the electrochemical storage of energy in capacitors.* Carbon, 2001. **39**(6): p. 937-950.

a

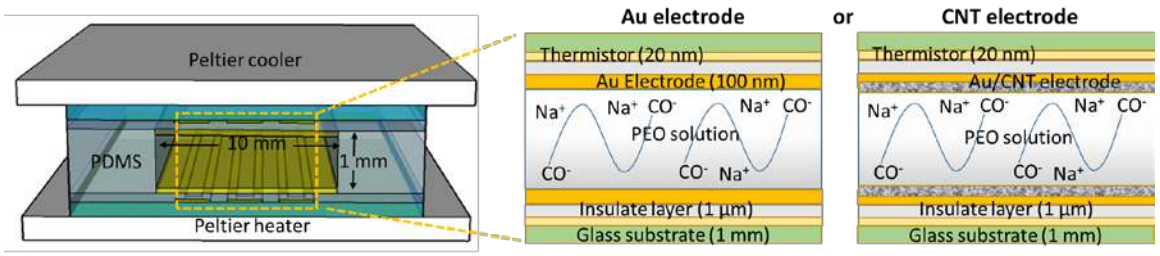

$$HO\text{-}(CH_2\text{-}CH_2\text{-}O)_n\text{-}OH + 2NaOH \rightarrow {}^{-}O\text{-}(CH_2\text{-}CH_2\text{-}O)_{n}\text{-}O^{-} + 2Na^{+} + H_2O$$

b

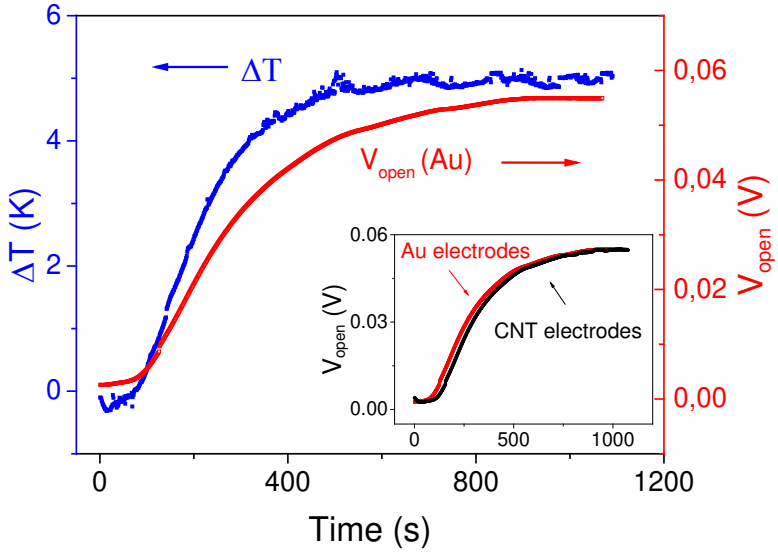

c

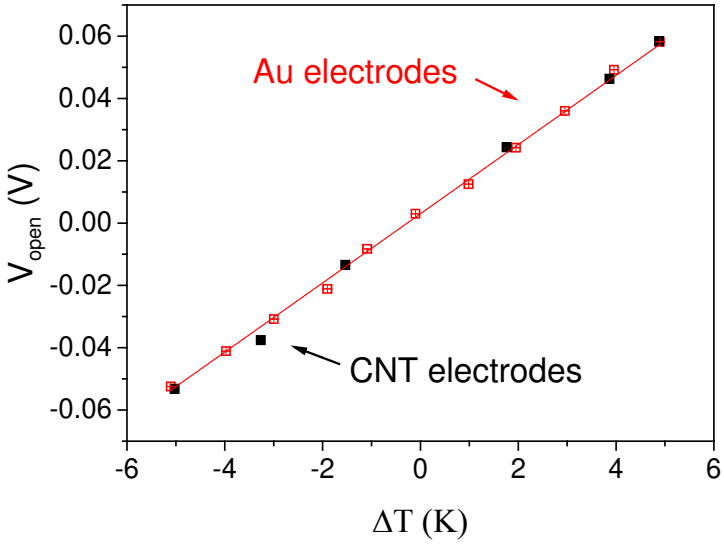

Figure 1 | Thermoelectric properties of PEO-NaOH solution.

a, Sketch of the ionic thermoelectric supercapacitor device (left) with two different electrodes (right, Au and CNT), and the reaction that takes place in the solution. **b**, Measured V_{thermo} and ΔT during heating using Au electrode, and the inset shows the measured V_{thermo} during heating using either Au or CNT electrodes. **c,** V_{thermo} at different ΔT using Au electrodes (red open squares) and CNT electrodes (black solid squares). For each point, ΔT is fixed until V_{thermo} was stable for at least 5 minutes. The slope of the linear fit to the data for the Au electrodes gives a Seebeck coefficient of 11.1 mV/K.

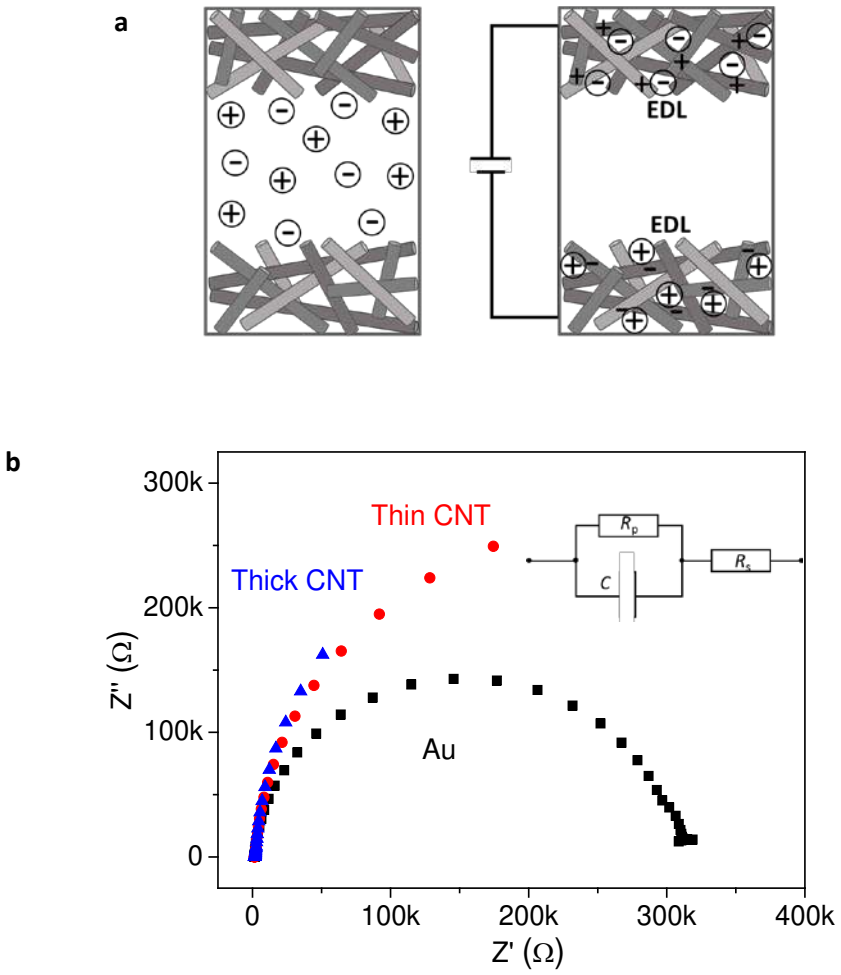

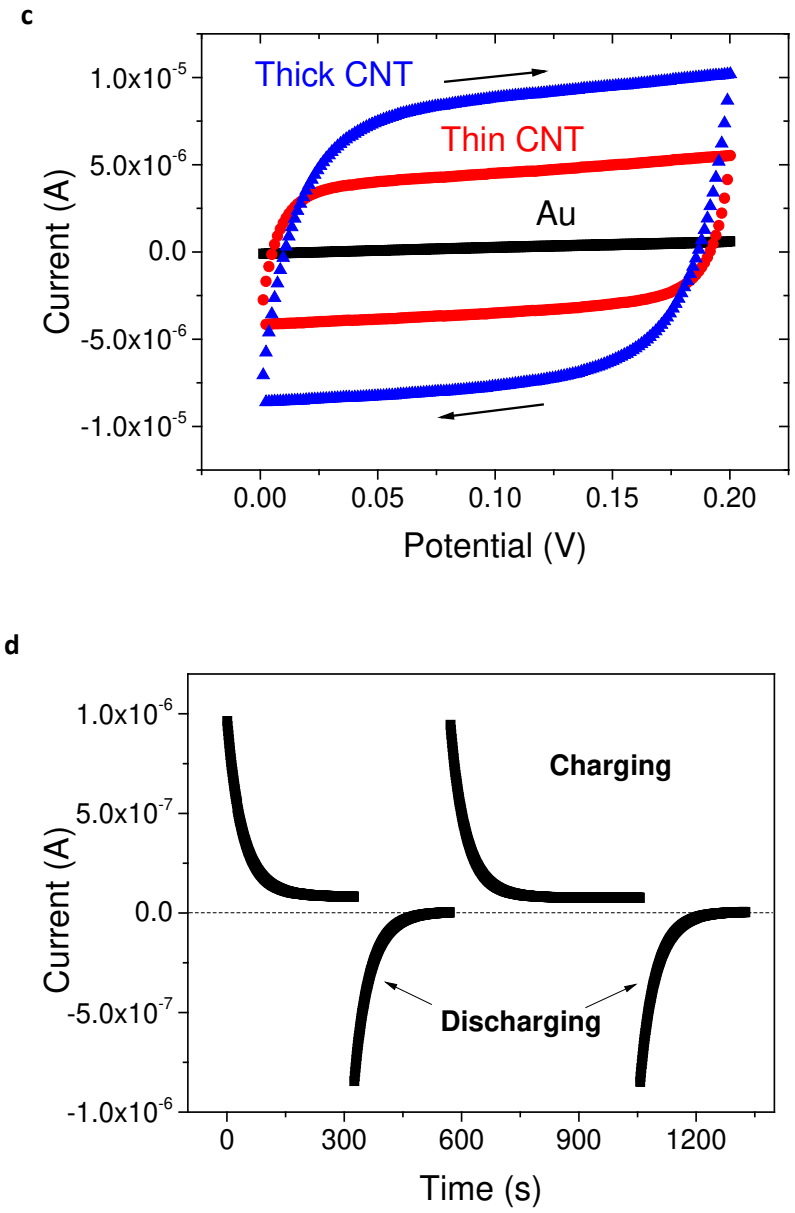

Figure 2 | Capacitance property of NaOH-PEO with CNT electrode.

a, Illustration of the electric double layer (EDL) formed in CNT eletrodes. **b,** Nyquist plot for devices with Au, thin CNT and thick CNT electrodes in the frequency range of 100 kHz to 1 mHz. The inset shows the simulated equivalent circuit: R_p: resistance connected parallel to the capacitance that is associated with the leakage current; R_s: resistance connected series which represents the internal resistance of the device; C: the capacitance. **c**, CV curves of devices with the three different types of electrodes, measured at 10 mVs^{-1}. **d,** Potential static electric charging and discharging of a device with thick CNT electrodes (R_{load}=50kΩ). All measurements are conducted at room temperature.

	Au	Thin CNT	Thick CNT
Capacitance (μF cm^{-2})	5.1	484	1031
R_s (Series resistance Ω)	1622	1545	1605
R_p(Parallel resistance Ω)	2.95 x 10^5	4.88 x 10^5	5.04 x 10^5

Table 1 |The parameters in equivalent circuit.

a

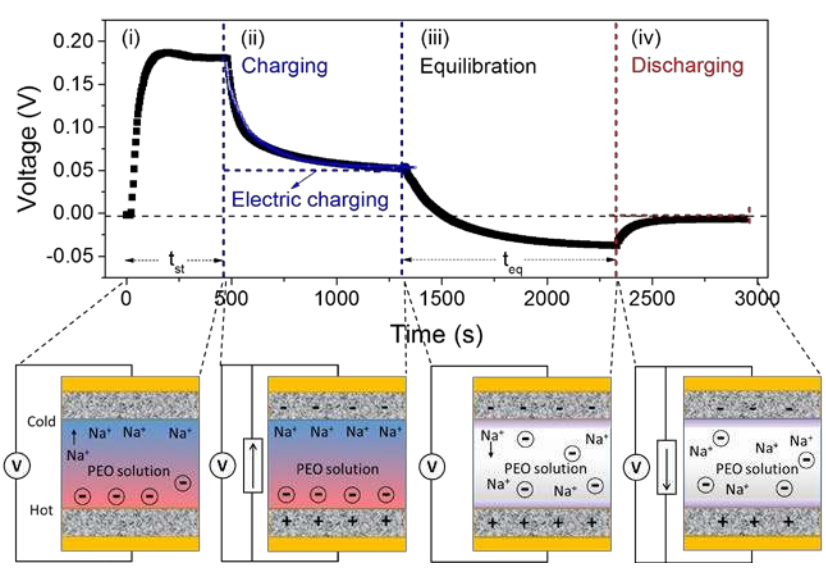

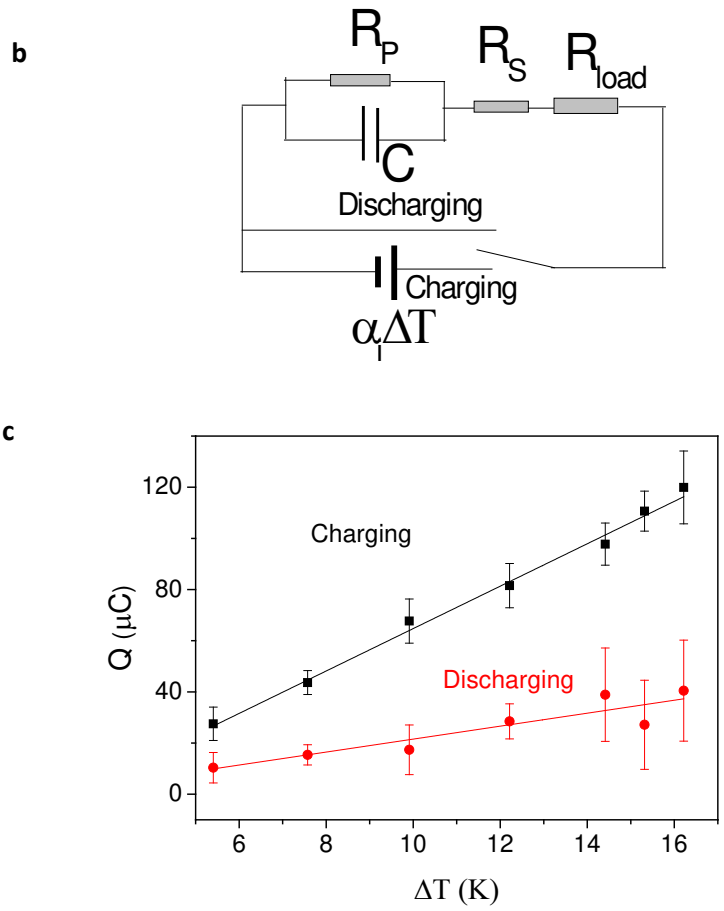

Figure 3 | Charging and discharging of ITESC.

a, Measured voltage curve (black) and mechanism sketch of a full charge and discharge cycle: (i) establishing the temperature gradient (ΔT=16 K) leads to an ionic thermovoltage, (ii) thermoelectric charging of the supercapacitor (the superimposed curve in blue corresponds to the electric charging of the same device upon applying an electric potential equals to the thermo-voltage value), (iii) equilibration to ΔT=0, and (iv) discharging (both with R_{load} = 100 KΩ). The inset shows the circuits used for charging and discharging. **b**, The equivalent circuit of charging and discharging process of ITESC. **c,** The amount of charge transferred to or from the capacitor during charging (black squares) and discharging (red circles) at different ΔT (R_{load} = 100 KΩ). The t_{eq} between charging and discharging was 400 -1200s.

	Electric-SC : thick CNT Discharge immediately	Electric-SC : thick CNT Discharge after 600 sec	ITESC: thick CNT Equilibration time: 550-650 sec
$Q_{charging}$ (C)	$2.42\times10^{-05}(\pm5{,}31\times10^{-07})$	2.42×10^{-05} $(\pm5{,}31\times10^{-07})$	2.50×10^{-05} $(\pm1{,}06\times10^{-06})$
$Q_{discharging}$(C)	2.28×10^{-05} $(\pm6{,}43\times10^{-07})$	$6.85\times10^{-06}(\pm2.24\times10^{-7})$	6.85×10^{-06} $(\pm9{,}25\times10^{-07})$

$Q_{discharging}/Q_{charging}$	94.2%	28.3%	27.4%

Table 2 |The amount of charge transferred to or from the capacitor during charging or discharging, for electric (Electric-SC) and thermoelectric (ITESC) charging for thick CNT capacitors ($V_{charging}$= 50 mV).

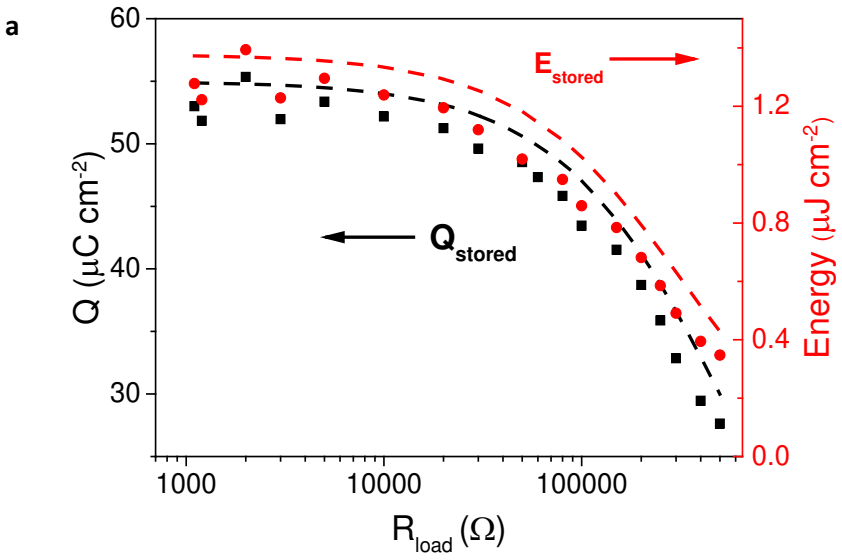

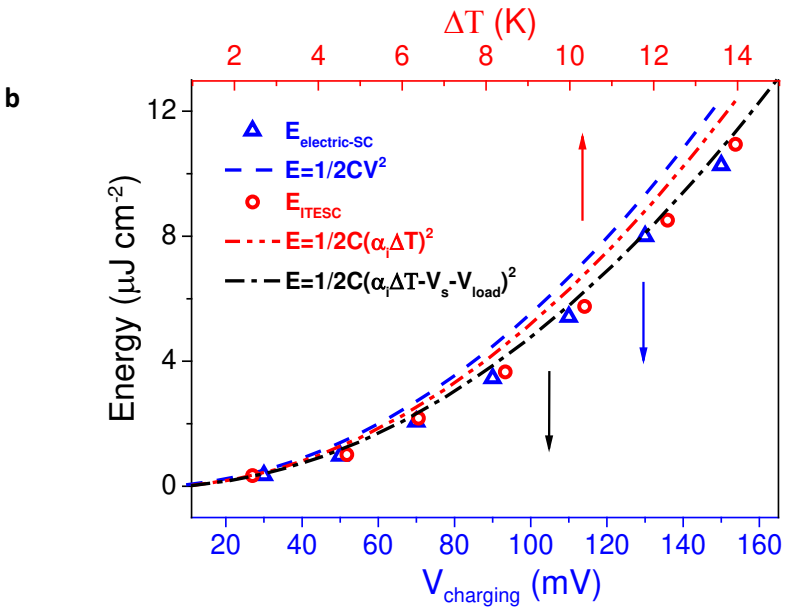

c

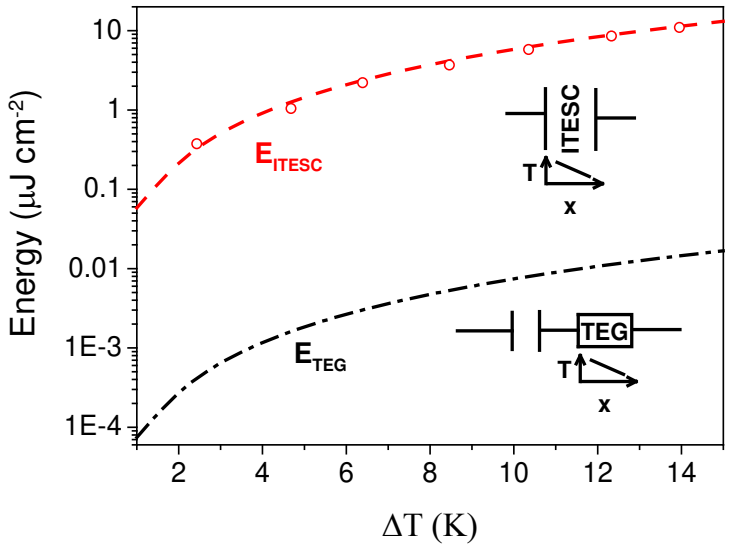

Figure 4 | Energy stored in the ITESC.

a, The amount of charge stored and electrical energy stored in the capacitor during charging for different R_{load} (ΔT = 4.5 K), the two dashed line represent the calculated value of the charge (black) and energy (red), respectively**. b,** Energy density versus ΔT for ITESC (red open circles), electric charging (blue open squares) and the theoretical prediction from V_{thermo} (dashed red line), $V_{electric}$ (dashed blue line), and $V_{effective}$ (dashed and dot black line). **c**, Energy density versus ΔT for ITESC, both experimental data (red open dot) and theoretical result (red dashed line), and theoretical prediction for the same SC charged by one leg of Bi_2Te_3 TEG (black dashed-dotted line).

Ionic Thermoelectric Supercapacitor

Dan Zhao, Hui Wang, Zia Ulla Khan, Jincan Chen*, Roger Gabrielsson, Magnus P. Jonsson, Magnus Berggren and Xavier Crispin

Department of Science and Technology,

Campus Norrköping, Linköping University,

S-60174 Norrköping, Sweden,

** Department of Physics, Xiamen University, People's Republic of China*

Supplementary Information includes:

1. **Chemical characterization of the PEO-NaOH electrolyte**
2. **Ionic Conductivity of the PEO-NaOH electrolyte**
3. **Fabrication and calibration of the reference electrodes**
4. **Effect of the dielectric constant on the Seebeck coefficient**
5. **Thermal conductivity measurement**
6. **Preparation of self-assembled CNT electrode on Au**
7. **Self-discharge of devices using both thick and thin CNT electrodes**
8. **Charging current comparison and control measurement using Au electrodes**
9. **Full mathematical framework to describe the equivalent circuit**
10. **Charging current**
11. **Efficiency**

1: Chemical characterization of the PEO-NaOH electrolyte

a) NMR characterization of the PEO-NaOH electrolyte

Proton nuclear magnetic resonance 1H spectra were recorded on Varian (300 MHz) spectrometer. The deuterated solvent was used as internal standard for DMSO-d6 (1H, δ = 2.50) were used as reference. [1] The NMR FID files were analyzed with MestReNova-9.1.0. All PEO samples were analyzed from 15% (w/w) PEO/DMSO-d6.

Table S1 below summarizes the 1H-NMR characterization of the different PEO-Na^+ complexes (entry A-D in Table S1) from the 1H-NMR spectra's (Figure S1). The region between 3.3 ppm and 3.6 ppm are related to hydrogen atoms that are belonging to the (-0-CH_2-CH_2-) polymer chains; while the region at 4.55ppm is identified as hydrogen atom belonging to alcohol end groups for the low molecular weight PEO. The degree of substitution (DS) of the PEO with alcohol end group is about 9%. The significant amount of alcohol groups is a key feature of this liquid polymer. The addition of 3% (w/w) of NaOH (~ 3 mol eq.) to the PEO-400 at rt. (entry B in Table S1) gives a 58% conversion of the alcohol groups -CH_2-OH to alkoxide groups -CH_2-O^-Na^+ through a condensation of water. Heating the same solution to 70 °C for two hours shifts this equilibrium by removal of water to reach a 77% conversion of alcohol protons to sodium ions (entry C in Table S1). Similar results, with metal ions (K^+ and Na^+) transfer ratio (mol%) from solid alkali metal salts of different anions to PEO-400 have been reported by others. [2] To further investigate the role of the anion transfer process on the degree of conversion of protons in PEO-400 to sodium ions, we added NaH (3% w/w, ~ 6 mol eq.) to the PEG-400. The resulting solution showed an almost complete conversion of the protons to sodium ions (entry D in Table S1). The 1H-NMR spectra in figure S1 also show the characteristic peak shifts for the remaining PEO-400 protons, moving from 4.5 ppm in pure PEO-400 to almost 5.5 in PEG/NaH due to PEO-O•••H•••O-PEO interactions, an effect usually seen in DMSO-d6. Although not shown, the 1H-NMR reveals a new contribution at 8.5 ppm upon the addition of NaOH and NaH to PEO, which is attributed to aldehyde groups emerging from the further oxidation of alkoxide groups.

Table. S1 The composition of different PEO-Na^+ complex.

Entry	**Solution composition**	**Peak areas – OH/OCH_2CH_2**	**DS[a]**	**PEG-$[OH]_x$ $[ONa]_y$**
A	Pure PEG	1/22	9.1	100%
B	PEG, NaOH (3% w/w)	1/52	3.8	PEG-$[OH]_{0.42}[ONa]_{0.58}$
C	PEG, NaOH (3% w/w), 70 °C, 2h	1/80	2.5	PEG-$[OH]_{0.23}[ONa]_{0.77}$
D	PEG, NaH (3% w/w)	1/778	0.26	PEG-$[OH]_{0.03}[ONa]_{0.97}$

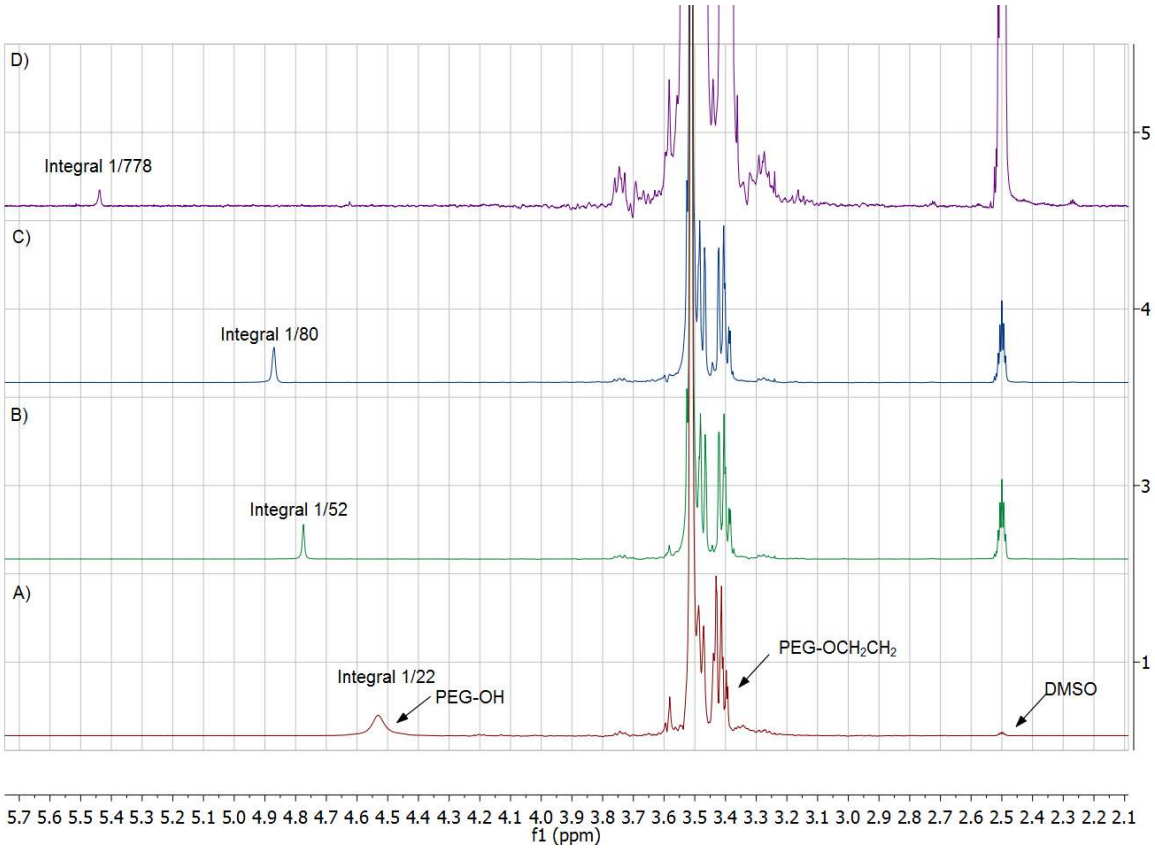

Fig. S1 ^{1}H-NMR spectras of A) Pure PEO, B) PEO-NaOH (3% w/w), PEO-NaOH (3% w/w), 70 °C, 2h, D) PEO-NaH (3% w/w)

b) FTIR characterization of the PEO-NaOH electrolyte

The FTIR (Fourier Transform Infrared Spectroscopy) spectrometer Equinox 55 from Bruker with the ATR (Attenuated Total Reflection) accessory A 225 having diamond crystal was used for studying the absorption of PEO and PEO-NaOH in the range of 400-4000 cm^{-1}. A drop of liquid material was placed on top of the diamond crystal and the measurements were run with 1 cm^{-1} increment for full range (400-4000 cm^{-1}) with 20 scans each time.

The FTIR spectra of pure PEO (Mw=400 g/mol) is compared with that of the PEO-NaOH that is used for the ITESC in the main text (Fig. S2). The PEO sample displays the same features as previously reported in the range 1400-1000 cm^{-1} [3]. As indicated by 1H-NMR; alcohols end moieties are in significant amount and clearly visible by the peak at 3450 cm^{-1} associated to OH stretching (black curve). Possible residual water might also contribute (green curve). Adding the NaOH leads to a decrease of that alcohol $–CH_2$-OH stretching peak around 3400 cm^{-1}, which is associated to the formation of alkoxide $–CH_2$-O^- Na^+: the proton of the alcohol group is removed by adding base. To further verify the result, we substitute NaOH to a stronger base, NaH, which possess higher deprotonating ability. From the result, it is clearly that the peak at 3450 cm^{-1} decrease even more which means most of the proton of the alcohol groups is almost totally removed by the base.

Note also that the presence of a small signal at 1650 cm^{-1} growing upon NaOH and NaH addition is attributed to C=O stretching in an aldehyde. This is supported by the presence of the 1H-NMR contribution at 8 ppm appearing also upon the addition of NaOH and NaH. Alcohol groups in PEO treated in harsh basic environment are known to be transformed from alkoxides to carboxylates (likely through an aldehyde intermediate) [4]. The contribution at 1750 cm^{-1} emerging upon the addition of extra water (green curve) is attributed to the creation of carboxylate groups [4]. In the PEO-NaOH electrolyte used in the ITESC device, the presence of carboxylate is vanishingly small.

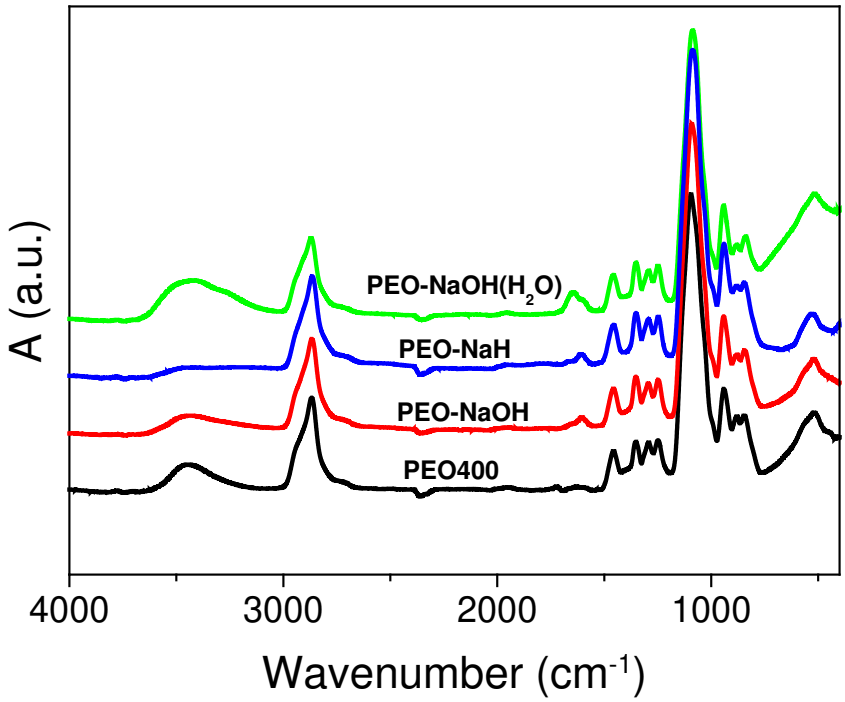

Fig. S2 ATR spectra of PEO (black), PEO-NaOH (70°C, red), PEO-NaH (blue) and PEO-NaOH (green) with a drop of water in the range 400-4000 cm^{-1}.

2: Ionic Conductivity of the PEO-NaOH electrolyte

Dielectric Spectroscopy is a powerful tool for characterizing the electrical and dielectric properties of liquids [5]. Three liquid materials (water, PEO, PEO-NaOH) were characterized inside a standard cell BDS1308 using the Impedance Spectrometer from Novocontrol in the frequency range of 0.1Hz to 10MHz with an input signal of $5mV_{rms}$. The measurements were carried out inside a climate chamber where the temperature was raised from 20 to 80°C with in steps of 10°C.

The Cole-Cole plots of the imaginary (Z´´) and the real part (Z´) of the impedance resemble typical parallel combinations of a resistor and capacitor (Fig. S3). The ionic conductivity was calculated from the first intercept of the high frequency semi-circle, where the response is fully resistive. It can be seen that the semicircle becomes smaller (the intercept is at a lower Z´) as the temperature rises, indicating an increase in the ionic conductivity of the media. For the PEO-NaOH mixture, the bulk conductivity

increases from 7.56E-05 S/cm at 20℃ to 1.96E-03 S/cm at 80℃ and from the Arrhenius plot, the activation energy was calculated to be 476 m eV for the PEO-NaOH mixture.

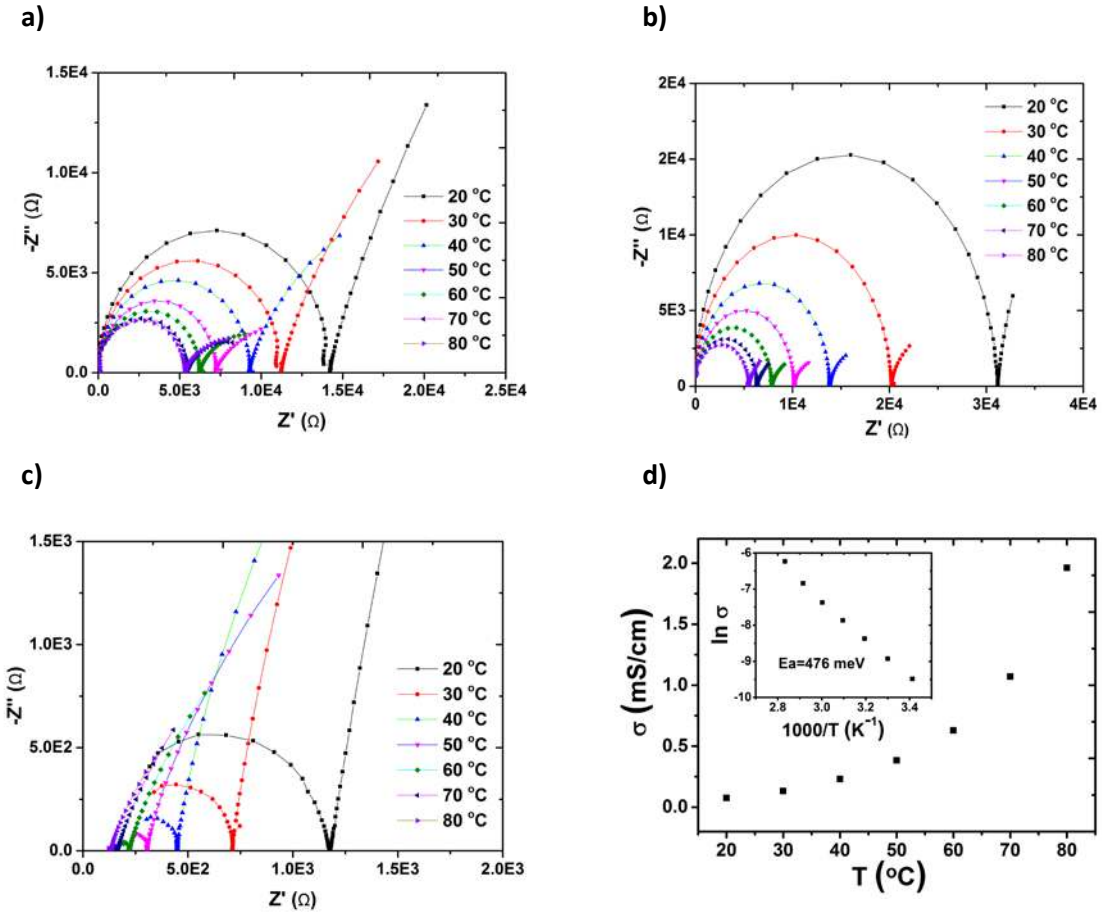

Fig. S3 Cole-Cole plot for **(a)** water (reference), **(b)** PEO and **(c)** PEO-NaOH. **(d)** The ionic conductivity in PEO-NaOH versus temperature (the inset is with other axis scale: log σ vs. 1000/T).

3: Fabrication and calibration of the reference electrodes

The two thermistors of the device consist of gold lines patterned on the substrate (10μm wide, 700mm long), and insulated from the top electrode with a thin (100nm) silicon nitride layer (1000nm). For calibration, the complete device with two thermistors is placed inside a climate chamber, and the two resistors (R_1 and R_2) are measured with four-point probes method using Keithley 2400 at different temperature. Temperature is set at 20, 25, 30, 35, 40℃, each for 20 min until the resistance keep constant. Fig. S4 shows the slope of the two curves are 88.8 Ω/K and 84.9 Ω/K, which promise an accurate conversion between resistance and temperature. Temperature difference $\Delta T=T_1-T_2$ between the electrodes during Seebeck measurement are subsequently estimated by measuring the resistance of the thermistors.

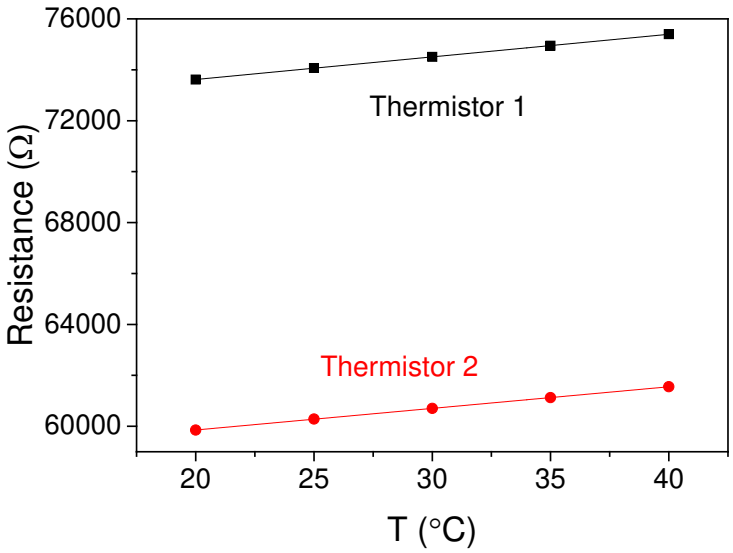

Fig. S4 Calibration curves as the resistance versus temperature for the reference electrodes.

4: Effect of the dielectric constant on the Seebeck coefficient

One question raised in the manuscript was about the effect of the dielectric constant on the heat of transport and Seebeck coefficient of ions. Indeed, the heat of transport of ions is known in aqueous solution [6, 7] but not in PEO. A first indication can be found by using the Born model. In this model, the heat of transport and thus the Seebeck coefficient due to one type of ions is related to both the dielectric constant ε and the variation in dielectric constant as a function of temperature ($d\varepsilon/dT$) is related to the Seebeck co-efficient as:[8]

$$S \propto \frac{d\varepsilon}{\varepsilon^2 dT} \tag{1}$$

Where ε is the complex dielectric constant of the medium and T is the temperature.

From the impedance data presented above (see Fig. S3) and the geometry of the cell, the real ($\acute{\varepsilon}$) and imaginary (ε'') parts of the dielectric constants were calculated using[9]:

$$\varepsilon' = \frac{Z'' L}{2\pi f \varepsilon_0 A Z^2} \tag{2}$$

$$\varepsilon'' = \frac{Z' L}{2\pi f \varepsilon_0 A Z^2} \tag{3}$$

Where L is the length of the cell; A is the area of each electrode; Z', Z'', Z are the real, imaginary and absolute values of the impedances; f is the frequency of the applied voltage; and ε_0 is the permittivity of free space (8.85E-12 F/m).

Fig. S5 displays the real part of the dielectric constant or relative permittivity ($\acute{\varepsilon}$) versus frequency for deionized water (reference) and PEO. The dielectric constant is huge at low frequency due to the formation of electric double layers with the metal electrodes [10]. At high frequency, such phenomenon is absent and the real part of the impedance reaches a constant value from which we

extract the static dielectric constant as $\acute{\varepsilon}$ at 1MHz. In order to check our set-up, we first consider DI water as reference. The measured value of the static dielectric constant was 80.6 at 20°C (Fig. S5a) which is very close to the reported value of $\acute{\varepsilon}$ (1MHz)=80.1 at the same temperature for pure water [11]. With the same cell, we characterized the PEO liquid (Fig. S5b) and the PEO-NaOH electrolyte (Fig. S5c) and found $\acute{\varepsilon}$ (1MHz) =36.1 and 42.5 respectively. We measured the properties at various temperatures and plotted the static dielectric constant versus temperature (Fig. S5d). The slope ($d\acute{\varepsilon}/dT$) for PEO is very small (0.02 K^{-1}) compared to that of water (0.497 K^{-1}). Hence, all in all, one can calculate the product $[d\acute{\varepsilon}/dT]/(\acute{\varepsilon}^2)$ (*Table 2*). According to Born's model, the heat of transport (and Seebeck contribution) by changing from water to PEO should be lower by 5 times. But we measure on the contrary a huge thermovoltage in PEO that cannot obviously be coming from a dielectric effect.

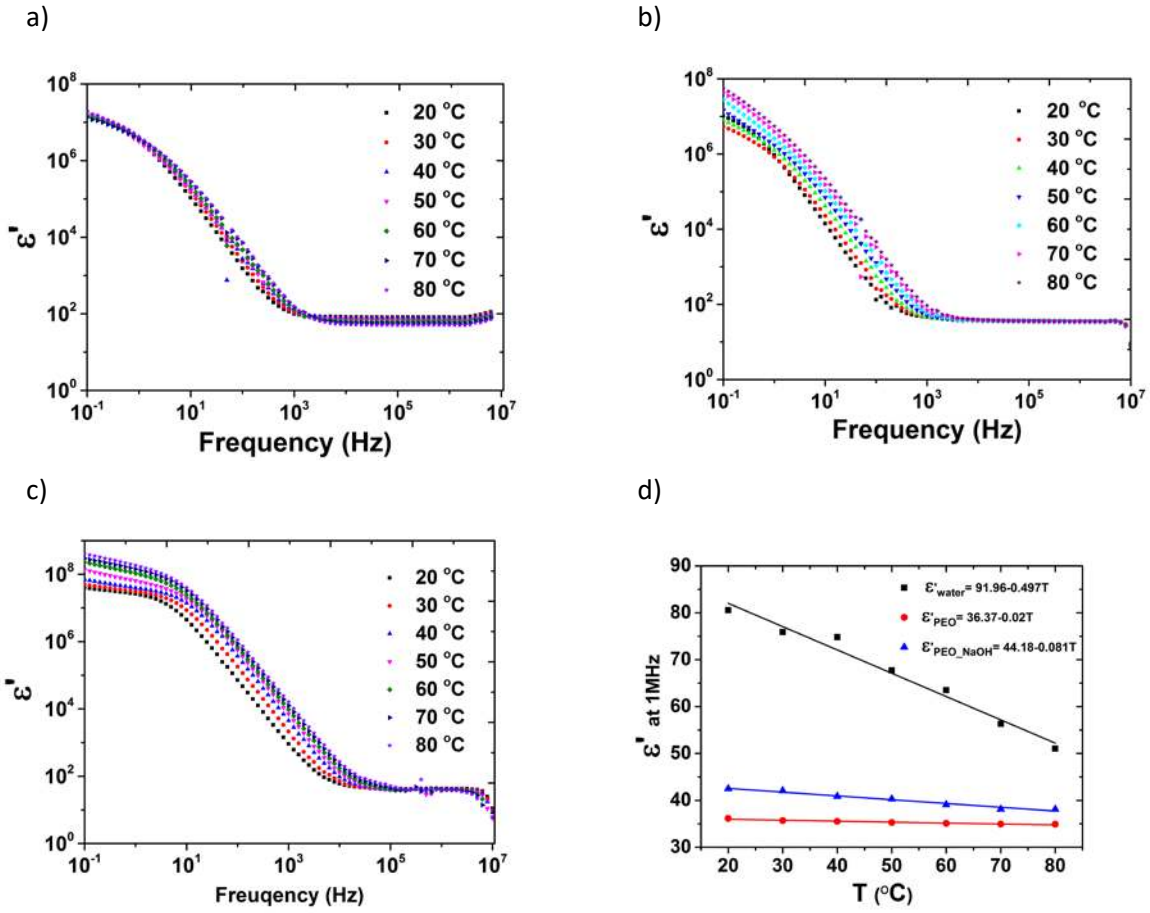

Fig. S5 Real part of the dielectric function as a function of frequency for **(a)** water, **(b)** PEO, **(c)** PEO-NaOH at different temperatures. **(d)** Static dielectric constant $\acute{\varepsilon}$ (1MHz) vs. temperature for the three liquids.

Table 2: The static dielectric constant $\acute{\varepsilon}$ of water, PEO, PEO-NaOH and their temperature dependency

Material	$\acute{\varepsilon}$ *at 20°C*	$d\acute{\varepsilon}/dT$ (K^{-1})	$[d\acute{\varepsilon}/dT]/(\acute{\varepsilon}^2)$ (K^{-1})
Water	80.6	-0.497	-7.65E-5
PEO	36.1	-0.02	-1.54E-5
PEO-NaOH	42.5	-0.081	-4.5E-5

5: Thermal conductivity measurement

The thermal conductivity of PEO-NaOH was measured by the three omega (3ω) method. We briefly describe the principle of this electrical method. The 3ω method was initially reported by D.G. Cahill et al. for the thermal conductivity measurement of amorphous materials[12]. A sinusoidal input current at frequency ω causes joule heating in the metal heater, which is in intimate contact with the substrate/material of choice. This causes a fluctuation in the resistance of the metal line at 2ω, which results in a voltage component modulated at 3ω at the terminals of the heater.

The temperature rise (ΔT) at the heater is given by[13]:

$$\Delta T = \frac{P}{\pi l \lambda} \int_0^\infty \frac{Sin^2(kb)}{(kb)^2 (k^2 + q^2)^{1/2}} dk \tag{4}$$

Where *P*, λ are the power input and the thermal conductivity, and *l* and *b* are the length and the half-width of heater, respectively. The thermal penetration depth (1/q) is defined as[12]:

$$\frac{1}{q} = \sqrt{\frac{\lambda}{i2\omega\rho C_p}} = \sqrt{\frac{D}{i2\omega}} \tag{5}$$

Where ρ, C_p and *D* stand for density, specific heat and thermal diffusivity, respectively. As the thermal penetration depth is inversely proportional to the frequency of the input current, it is always necessary to check that the thermal wave remains well within the material at the lowest applied frequency to avoid scattering at the gas-sample boundary.

D.G. Cahill simplified the equation as[9]:

$$\Delta T = \frac{P}{\pi l \lambda} \left[\frac{1}{2} ln \frac{D}{r^2} + ln2 - 0.5772 - \frac{1}{2} ln(2\omega) - \frac{i\pi}{4} \right] \tag{6}$$

Dong-Wook Oh et al.[11] utilized another device architecture designed for the thermal conductivity measurement of liquid samples. We have been inspired by this approach and used it to measure the thermal conductivity of PEO-NaOH solution. The liquid material is filling a plastic cavity designed right above the metal heater deposited on a glass substrate. The temperature oscillation of the heater (ΔT_f) due to the heat transport into liquid material in the cavity can be estimated by subtracting the effect of the substrate as follows[11]:

$$\frac{1}{\Delta T_{s+f}} = \frac{1}{\Delta T_s} + \frac{1}{\Delta T_f} \tag{7}$$

Where ΔT_s is temperature oscillation only with glass and the insulation layer with empty cavity, ΔT_{s+f} is the temperature oscillation of the heater with glass substrate and filled cavity; while ΔT_f is the calculated temperature oscillation due to the heat transported only into the material in the cavity. ΔT_f is used to calculate the thermal conductivity of the PEO-NaOH under study.

We here describe briefly the fabrication and the dimension of the Au heater on the glass substrate. The glass substrate was coated with 15 nm chrome (Cr) and 140 nm gold (Au) and patterned by photolithography to get a 3 mm long and 20 µm wide Au line (the heater-thermometer). This metal line was then insulated with a 2 µm thick UV cured SU8 layer. The metal heater-thermometer was first calibrated inside a climate chamber by varying the temperature from 20°C to 50°C. Then in order to measureΔT_s, the glass sample with insulation and empty cavity was placed inside a vacuum cryogenic probe station (Janis Research) to avoid gas convection effect. An input AC current was applied from a waveform generator (3022C Tektronix) and the 3ω voltage was measured by a Lock-in Amplifier (SR850 Stanford Research) with a precision difference amplifier AD8279 for signal conditioning. The measured 3ω voltage was translated to ΔT_s by[14]:

$$\Delta T_s = 2\frac{V_{3\omega}}{I}\frac{\partial T}{\partial R} \tag{8}$$

The results of ΔT vs. *ln2ω* are plotted in Fig. S6 for empty and the cavity filled with different materials. All the 3ω measurements were carried out with the same input current for the same frequency range. The cavity was 1 cm tall and it was filled with 2 mL of liquid in each case. It can be seen in all measurements that the total temperature oscillation ΔT_{s+f} is smaller than ΔT_s since part of the heat generated by the heater penetrates into the solution. The temperature oscillation ΔT_f due to the heat propagated into solution only was calculated using equation (8) and the thermal conductivity was calculated from a linear fit of ΔT_f vs. *ln2ω*. The validity and accuracy of our experimental setup was first tested with known materials (DI water and ethylene glycol (EG)). Two measurements were carried out by filling the cavity with water and then with ethylene glycol (EG). The measured values of the thermal conductivities of 0.632 $Wm^{-1}K^{-1}$ (water) and 0.272 $Wm^{-1}K^{-1}$ (EG) are in agreement with the reported values of 0.6 $Wm^{-1}K^{-1}$ and 0.27 $Wm^{-1}K^{-1}$ [11]. Hence, the measurement setup was trustable with an uncertainty of ±5%. Finally, the cavity was filled with PEO and then with PEO-NaOH and the calculated thermal conductivities were 0.191 $Wm^{-1}K^{-1}$ and 0.216 $Wm^{-1}K^{-1}$, respectively.

a)

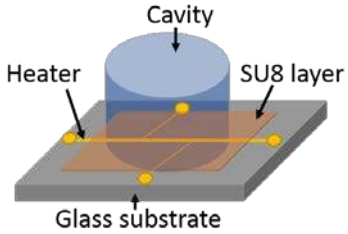

b)

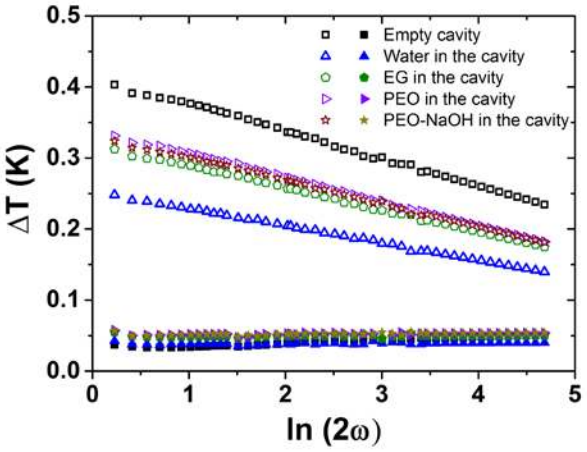

Fig. S6 **(a)** Sample structure, **(b)** Temperature oscillation on the gold (Au) heater. Empty symbols are for the in phase and filled symbols are for the out of phase components of *ΔT*.

6: Preparation of self-assembled CNT electrode on Au

CNT was dispersed in water to form a 0.1 % concentration solution, and exposed to ultrasonic treating for 30 min. The Au electrodes were pretreated by UV plasma for 3 min, and placed on a hot plate set at 105°C. Next, a certain amount of CNT solution is dipped on Au electrode during heating (30 µL for thin CNT electrodes, and 60 µL for thick CNT electrodes). After water evaporation, the CNT attached to the surface of Au due to hydrophobic forces between the two. The prepared electrodes were rinsed by acetone and water before use.

7: Self-discharge of devices using both thick and thin CNT electrodes

The self-discharge is investigated in detail by monitoring the open voltage (V_{open}) of the capacitors after electrical charging. As shown in fig S7, devices with thin and thick CNT electrodes are charged electrically at three different potentials (50 mV, 100 mV and 150 mV). Next, the circuit is cut and V_{open} is recorded versus time. Initially, V_{open} decreases rapidly, especially for the devices with thin CNT eletrodes. And the inset figure shows that for the same electrodes, the decay rate of different charging potential are similar.

The electrically charged SCs, which could be discharged directly (time=1 s) after charging, provide $Q_{discharge}/Q_{charge}$ of 94% and 83% for the thick and thin CNT electrode devices, respectively (see table 1). However, if discharging is triggered after a time equal to the equilibration time t_{eq}, i.e. accounting for the self-discharge, this gives $Q_{discharge}/Q_{charge}$ of 28% (thick CNT electrodes), which is very close to the measured 27% in the ITEC. Since the thick CNT electrode possess more compensate charge during charging, it needs longer time for self-discharge. This explains why the delay curve is sharper for the thin electrode than the thick CNT electrode.

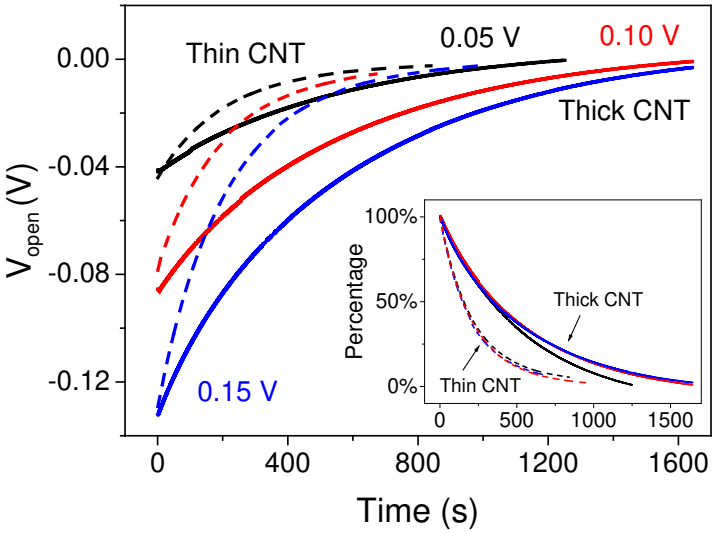

Fig. S7 Decay of V_{open} after electrical charging at 0.15 V (blue), 0.10 V (red) and 0.05 V (black), for supercapacitors based on thin (dashed lines) and thick (solid lines) CNT electrodes.

8: Charging current comparison and control measurement using Au electrodes.

The charging current is measured for both electric and thermoelectric charging. For thermoelectric charging, ΔT=4.5 K gives a V_{thermo} of 0.05 V. After V_{thermo} has stabilized, the load resistance is connected. For electric charging, the charging potential is set the same as V_{thermo} for thermoelectric charging (0.05 V). The device is placed in a climate chamber to keep the same temperature as $T_{average} = \frac{T_{hot}+T_{cold}}{2}$. From the results shown in fig. S8 a, the charging behavior and leakage current of the two methods are almost the same.

Fig. S8 b shows the charging and discharging performance of a device with Au electrodes (no CNTs). After connecting R_{load}, V_{thermo} drops immediately because of the small capacitance. Because there are no compensate charges on the electrodes, V_{thermo} tends to first approach its original value and then decrease to zero when R_{load} is disconnected and the heat is turned off.

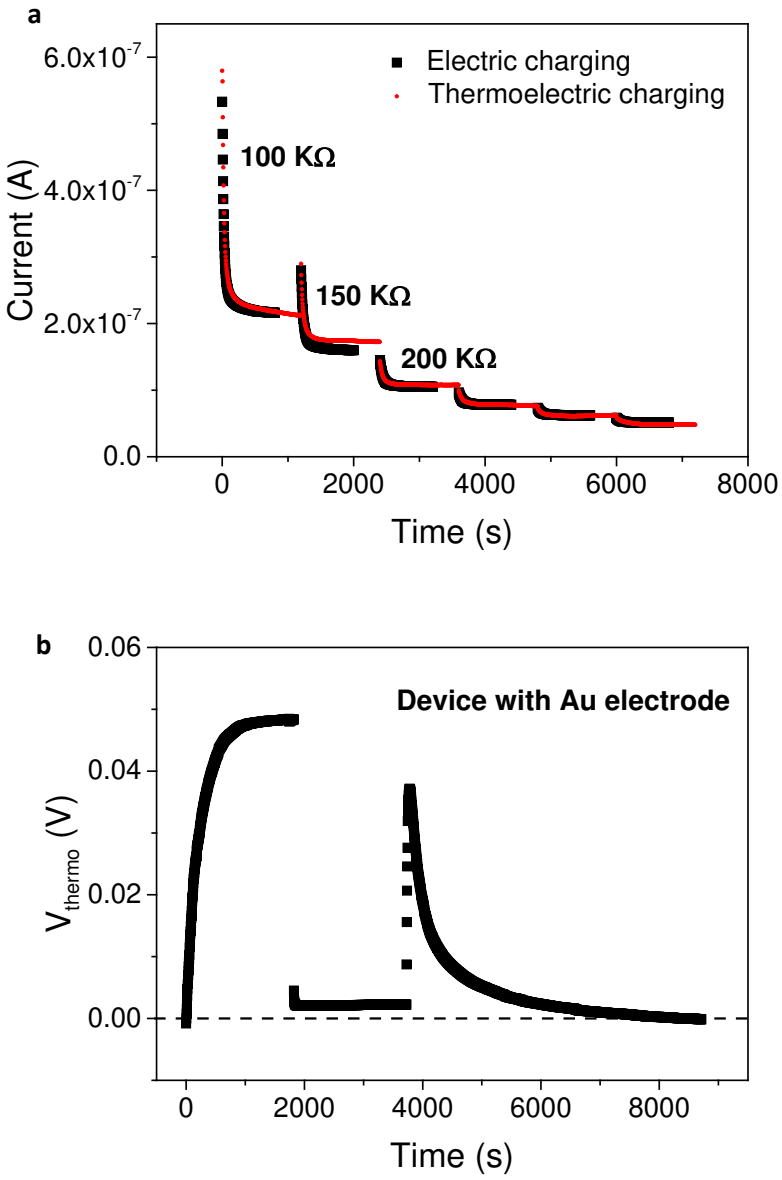

Fig. S8 **(a)** Comparison between electric and thermoelectric charging current for different R_{load}. **(b)** Charging and discharging measurement using Au electrodes.

9: Full mathematical framework to describe the equivalent circuit

According to the equivalent circuit, the charging electric current $I(q_{ch} = \frac{dq_{ch}(t)}{dt})$ and the discharging electric current $I(q_{dis}) = -\frac{dq_{dis}(t)}{dt} = -C\frac{dV_{dis}(t)}{dt}$ can be calculated from the following equations:

$$(R_s + R_{load})\frac{dq_{ch}(t)}{dt} + [1 + \frac{(R_s + R_{load})}{R_P}]\frac{q_{ch}(t)}{C} = \alpha_i \Delta T \qquad (1)$$

From Eq. (1), we can obtain

$$q_{ch}(t) = q_{ch}(0)\exp\{-[\frac{1}{C(R_s + R_{load})} + \frac{1}{CR_P}]\}t$$
$$+\frac{\alpha_i \Delta T / (R_s + R_{load})}{\frac{1}{C(R_s + R_{load})} + \frac{1}{CR_P}}\left(1 - \exp\{-[\frac{1}{C(R_s + R_{load})} + \frac{1}{CR_P}]\}t\right) \quad \text{Eq. 2a}$$

$$\tau = \frac{C(R_S + R_{load})R_p}{R_S + R_{load} + R_p}, \text{ when } R_P >> (R_s + R_{load}), \tau = C(R_s + R_{load}). \quad \text{Eq. 2b}$$

$$q_{ch}(t) \approx q_{ch}(0)\exp(-t/\tau) + C\alpha_i \Delta T[1 - \exp(-t/\tau)] \quad \text{Eq. 2c}$$

In the experimental charging and discharging processes, t is finite. $q_{ch}(0) > 0$ except for the first charging process. $q_{ch}(0)$ is dependent on the time of the charging and discharging processes. We take 5 times of τ as the charging and discharging time, for during this period, 99% of the charge has been transferred.

10: Charging current

The voltage across R_{load} is measured for different R_{load}, and the charging current is obtained by $I = \frac{V}{R_{load}}$. To calculate the amount of charge and energy stored in the device, the curve of the current is integrated for the charging period. For each R_{load}, the complete charging time is considered as 5 times of the time constant (τ).

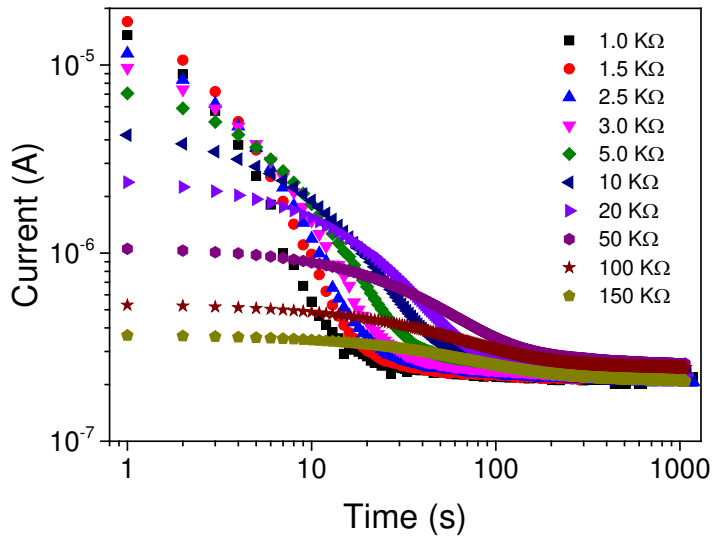

Fig. S9 Current generated during charging for serious R_{load}, plotted with time.

11: Efficiency

Heat-to-electricity charging conversion efficiency

We evaluate the efficiency of the ITESC in converting heat to electricity through the charging efficiency. The charging efficiency is defined as the ratio between the electrical energy that is generated and stored in the ITESC from the charging (E_{out}, term A below) and the total heat that is required to achieve that storage and hence, the total heat absorbed over one full ITESC cycle (Q_{in}). Experimentally, A is measured as the integrated current through R_{load} minus the leakage current during charging (step ii in Fig 3a), $\frac{1}{2C}\left(\int_0^{t_{ch}} I_{ch}dt\right)^2$. Term A can also be calculated from the measured device capacitance and the effective charging voltage as $\frac{1}{2}C[\Delta T\alpha_{\text{i}} - V_{load} - V_s]^2$.

$$\eta = \frac{E_{out}}{Q_{in}} = \frac{\frac{1}{2}C[\Delta T\alpha_{\text{i}} - V_{load} - V_s]^2}{\frac{1}{2}mC_h\Delta T + \kappa\frac{A}{L}\int_0^{t_{st}}\Delta T dt + \kappa\frac{A}{L}\int_{t_{st}}^{t_{ch}}\Delta T dt - \frac{1}{4}\frac{R_s C(\Delta T\alpha_{\text{i}} - V_{load} - V_s)^2}{R_{load}} + CT_h\alpha_i^2\Delta T}$$

$$= \frac{A}{B+C1+C2+D+E} \qquad (3)$$

Q_{in} has several types of contribution. First, $\frac{1}{2}mC_h\Delta T$ (term B) is the heat absorbed by the PEO-NaOH electrolyte (mass m=9.4×10^{-2}gr, specific heat C_h= 2.13 Jg^{-1}K^{-1} (from the datasheet of DOW chemical company) upon increasing the average temperature of the electrolyte (note that the mass of the electrodes is negligible ~10^{-6}gr compared to the mass of PEO-NaOH). Second, the Fourier contribution $\kappa\frac{A}{L}\int_0^{t_{st}}\Delta T dt$ (term C1) corresponds to the heat flow during the time to establish the steady-state thermovoltage (step i in Fig. 3a) and the term C2 is the heat flow during charging. The thermal conductivity κ of PEO-NaOH is 0.21Wm^{-1}K^{-1}. Third, the Joule effect (term D), equal to $\frac{1}{4}\frac{R_s R_p C(\Delta T\alpha_{\text{i}} - V_{load} - V_s)^2}{(R_{load}+R_s)(R_{load}+R_s+R_p)}$, will bring back part of the energy and lower the absorbed heat. Experimentally, we measure term E as $\frac{1}{2}R_s\int_0^{t_{ch}} I_{ch}^2 dt$, where R_s is the internal resistance of the ITESC and I_{ch} is the charging current equals to I_{load}-$I_{leakage}$. Finally, the ionic current also lead to a small Peltier heat contribution $CT_h\alpha_i^2\Delta T$ measured as $\alpha_i T_h\int_0^{t_{ch}} I_{ch}dt$ (term E). The charging efficiency for different R_{load} is shown in Fig. S11 a (symbols are from the current measurement and lines are from calculation) for ΔT=4.5 K and reaches 6× 10^{-6} % at low R_{load}.

We compare the efficiency of the ITESC with that of a circuit composed of a SC connected in series with a conventional TEG. In that case, we take a TEG of the same area and volume as the ITESC but made of Bi_2Te_3 and submitted to ΔT=4.5K. Using the same heat power for ITESC, we have measured the time needed to establish a constant open circuit potential (t_{st}) for the Bi_2Te_3 leg to be 10 times lower than for the ITESC of the same dimension. This time t_{st} for Bi_2Te_3 is limited by the heat diffusion; while for the ITESC t_{st} is limited by the ionic thermodiffusion (slower than the heat diffusion). Using the material properties of Bi_2Te_3 (C_h= 0.153Jg^{-1}K^{-1}, m=0.60g, κ=1.2Wm^{-1}K^{-1}), we calculate the new terms B, C1 and C2. As far as the terms A, D and E are concerned, we assume this is from SC based on CNT and PEO-NaOH (see main text section 2) but charged with the thermovoltage of the TEG. As shown in Figure S10 a, the efficiency of the TEG-SC (curve iii) is more than 2500 times lower than the efficiency of the ITESC (curve i).

Since this is the first ITESC and that we don't have optimized its architecture, the efficiency is far from what may be provided by future devices. In order to investigate the potential for

improvement, we plot the various energetic contributions corresponding to the terms in equation 3 (Fig. S10 b). The dominating contribution is from the heating energy (term C), because the time needed for the electrolyte to reach a stable V_{open} (t_{st}) is relatively long. In turn, t_{st} can likely be decreased by a factor of 10000 by reducing the length of the electrolyte leg from 1 mm to 10µm. Because the time needed to reach steady thermovoltage (t_{st}, region i in Fig 3a) depends quadratically on the length of the leg since this is a diffusion limited phenomenon [15]. Note that with an active external cooling power of 8W, a temperature gradient ΔT=4.5K is obtained over a 10 µm long PEO-NaOH leg. Simultaneously, the heat flux will increase by a factor of 100 due to Fourier equation: $Q = \kappa A \frac{\Delta T}{L}$. Hence, decreasing the length by two orders of magnitude leads to two orders of magnitude reduction of C1. Replacing the 1 mm long leg with a 10 µm long leg leads to a reduction in term B; which results in an enhancement of efficiency from 6×10^{-6}% to 3×10^{-4}% (curve ii). We now turn to the efficiency of the TEG-SC circuit, using the material parameters for Bi_2Te_3 for a 10µm long leg of the same volume as PEO-NaOH in ITESC. Note that because of the higher thermal conductivity, a cooling power of 48W is now required to get a temperature gradient of 4.5K. The efficiency of the TEG-SC (curve iv) reaches 2×10^{-8} % and is around 11000 times lower than the ITESC (curve ii).

Fig. S10 c reports the predicted evolution of the efficiency (with a 10 µm long leg) over the wide range of temperature gradient (0-100°C). Because the numerator in Equation 4 scales as ΔT^2 and the denominator is dominated by the terms B+C1+C2, which are proportional to ΔT, the resulting efficiency is linearly increasing with ΔT. It is important to keep in mind that the required external cooling-heating power increases proportionally with ΔT, so ΔT=100°C would require 177W. We observe that the efficiency increases with ΔT to around 0.01% at ΔT=100°C. The efficiency for TEG-SC also increases with ΔT, however, remains more than three orders of magnitude lower than the efficiency of the ITESC for all investigated ΔT. Moreover, for electrolyte possesses higher conductivity, which means a lower Rs, the time needed for fully charging will be shortened. And this will result an enhancement of efficiency to 0.08%.

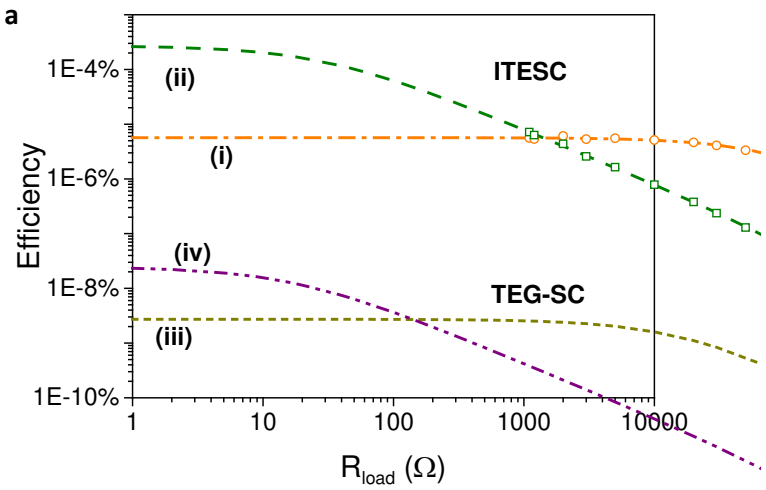

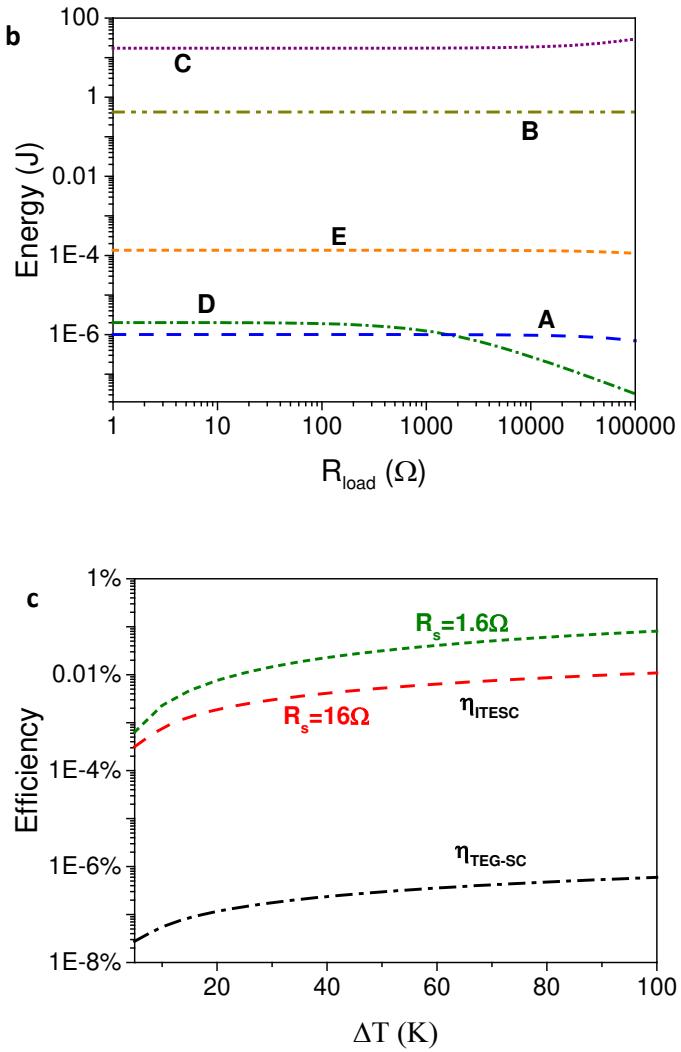

Fig. S10 (a) The efficiency of ITESC and TEG-SC for different R_{load} with consideration of: the length of leg we are using (i: ITESC, iii: TEG-SC); the length of leg is reduced from 1 mm to 10 µm (ii: ITESC, iv: TEG-SC). **b**, The contribution of the four different parts of the input energy, and the output energy. **c,** Predicted efficiency of ITESC (red dashed line) and TEG-SC (black dashed-dotted line) versus Δ*T*, and electrolyte of 10 times higher conductivity (green short dashed line), with leg length of 10 µm.

References:

1. Gottlieb, H.E., Kotlyar, V. & Nudelman, A. NMR chemical shifts of common laboratory solvents as trace impurities. *J Org Chem*. **62.** 7512-7515 (1997)
2. Chen, J., Spear, S. K., Huddleston, J. G. & Rogers, R. D. Polyethylene glycol and solutions of polyethylene glycol as green reaction media. *Green. Chem*., **7**, 64-82 (2005)

3. Su, Y.l., Wang, J. & Liu,H.Z. FTIR spectroscopic investigation of effects of temperature and concentration on PEO−PPO−PEO block copolymer properties in aqueous solutions. *Macromolecules*, **35**, 6426-6431 (2002)
4. Xiao, Y., Jiang, J. & Huang, H. *C*hemical dechlorination of hexachlorobenzene with polyethylene glycol and hydroxide: Dominant effect of temperature and ionic potential. *Scientific reports*, **4**. DOI:10.1038/srep06305 (2014)
5. Blythe, A.R. & Bloor, D. Electrical properties of polymers2005: Cambridge University Press.
6. Agar, J., Mou, C. & Lin, J.L. Single-ion heat of transport in electrolyte solutions: a hydrodynamic theory. *The Journal of Physical Chemistry*. **93**(5) 2079-2082 (1989)
7. Sokolov, V., Kobenin,V. & Usatchova, I. The standard entropy of transport of potassium chloride in the water–methanol system at 298 K*. Physical Chemistry Chemical Physics* **1**(12) 2985-2987 (1999)
8. Bonetti, M., Nakamae, S., Roger, M. & Guenoun, P. Huge Seebeck coefficients in nonaqueous electrolytes*. The Journal of chemical physics*, **134**(11) 114513 (2011)
9. Lanfredi, S. & Rodrigues, A. Impedance spectroscopy study of the electrical conductivity and dielectric constant of polycrystalline $LiNbO_3$. *Journal of applied physics,* **86**(4) 2215-2219 (1999)
10. Bordi, F., Cametti, C. & Colby, R. Dielectric spectroscopy and conductivity of polyelectrolyte solutions*. Journal of Physics: Condensed Matter*, **16**(49) R1423 (2004)
11. Malmberg, C. & Maryott, A. Dielectric Constant of Water from 00 to 1000 C*. Journal of research of the National Bureau of Standards*, **56** 1-8 (1956)
12. Cahill, D.G. & Pohl, R.O. Thermal conductivity of amorphous solids above the plateau*. Physical Review B*, **35**(8) 4067-4073 (1987)
13. Cahill, D.G., Thermal conductivity measurement from 30 to 750 K: the 3ω method*. Review of Scientific Instruments*, **61**(2) 802-808 (1990)
14. Oh, D.W., Jain, A., Eaton, J. K., Goodson, K. E., & Lee J. S. Thermal conductivity measurement and sedimentation detection of aluminum oxide nanofluids by using the 3ω method. *International Journal of Heat and Fluid Flow*, **29**(5) 1456-1461 (2008)
15. Atkins, P. and J. de Paula, *Atkins' Physical Chemistry*. 2010: OUP Oxford.